

The first 62 AGN observed with SDSS-IV MaNGA – III: stellar and gas kinematics

Gabriele S. Ilha,^{1,2*} Rogemar A. Riffel,^{1,2} Jaderson S. Schimoia,^{1,2,3}
 Thaisa Storchi-Bergmann,^{3,2} Sandro B. Rembold,^{1,2} Rogério Riffel,^{3,2}
 Dominika Wylezalek,⁴ Yong Shi,⁵ Luiz N. da Costa,^{2,6} Alice D. Machado,^{1,2}
 David R. Law,^{7,8} Dmitry Bizyaev,^{9,10} Nicolas D. Mallmann,^{3,2} Janaina Nascimento,^{3,2}
 Marcio A. G. Maia,^{2,6} Rafael Cirolini^{1,2}

¹Departamento de Física, CCNE, Universidade Federal de Santa Maria, 97105-900, Santa Maria, RS, Brazil

²Laboratório Interinstitucional de e-Astronomia - LIneA, Rua Gal. José Cristino 77, Rio de Janeiro, RJ - 20921-400, Brazil

³Departamento de Física, IF, Universidade Federal do Rio Grande do Sul, CP 15051, 91501-970, Porto Alegre, RS, Brazil

⁴European Southern Observatory, Karl-Schwarzschildstr 2, 85748 Garching bei München, Germany

⁵Department of Astronomy, Nanjing University, Nanjing 210093, China

⁶Observatório Nacional - MCT, Rua General José Cristino 77, Rio de Janeiro, RJ - 20921-400, Brazil

⁷Space Telescope Science Institute, 3700 San Martin Drive, Baltimore, MD 21218, USA

⁸Dunlap Institute for Astronomy and Astrophysics, University of Toronto, 50 St. George Street, Toronto, Ontario M5S 3H4, Canada

⁹Apache Point Observatory, PO Box 59, Sunspot, NM 88349, USA

¹⁰Sternberg Astronomical Institute, Moscow State University, 119992 Moscow, Russia

Accepted XXX. Received YYY; in original form ZZZ

ABSTRACT

We investigate the effects of Active Galactic Nuclei (AGN) on the gas kinematics of their host galaxies, using MaNGA data for a sample of 62 AGN hosts and 109 control galaxies (inactive galaxies). We compare orientation of the line of nodes (kinematic Position Angle – PA) measured from the gas and stellar velocity fields for the two samples. We found that AGN hosts and control galaxies display similar kinematic PA offsets between gas and stars. However, we note that AGN have larger fractional velocity dispersion σ differences between gas and stars [$\sigma_{\text{frac}} = (\sigma_{\text{gas}} - \sigma_{\text{stars}})/\sigma_{\text{stars}}$] when compared to their controls, as obtained from the velocity dispersion values of the central (nuclear) pixel (2.⁵ diameter). The AGN have a median value of σ_{frac} of $<\sigma_{\text{frac}}>_{\text{AGN}} = 0.04$, while the median value for the control galaxies is $<\sigma_{\text{frac}}>_{\text{CTR}} = -0.23$. 75 % of the AGN show $\sigma_{\text{frac}} > -0.13$, while 75 % of the normal galaxies show $\sigma_{\text{frac}} < -0.04$, thus we suggest that the parameter σ_{frac} can be used as an indicative of AGN activity. We find a correlation between the [O III] $\lambda 5007$ luminosity and σ_{frac} for our sample. Our main conclusion is that the AGN already observed with MaNGA are not powerful enough to produce important outflows at galactic scales, but at 1-2 kpc scales, AGN feedback signatures are always present on their host galaxies.

Key words: galaxies: active – galaxies: kinematics and dynamics – galaxies: general

1 INTRODUCTION

Theoretical studies and numerical simulations suggest that Active Galactic Nuclei (AGN) play an important role in the evolution of their host galaxies (e.g. Hopkins et al. 2005). Currently, it is widely accepted that galaxies with spherical component (bulge of spiral galaxies and elliptical galaxies) host a central supermassive black hole (SMBH, Ferrarese & Merritt 2000; Gebhardt et al. 2000; Tremaine et al. 2002; Scannapieco et al. 2005) and cosmo-

logical simulations that do not include feedback effects from the SMBH result in galaxy stellar masses much higher than observed (Di Matteo et al. 2005; Springel et al. 2005; Bower et al. 2006). Massive outflows originated in the accretion flow are claimed to regulate and couple the growth of the galactic bulge and SMBH (Hopkins et al. 2005) and to explain the relation between the mass of the SMBH and stellar velocity dispersion of the bulge – the $M - \sigma$ relation (e.g. Ferrarese & Merritt 2000; Gebhardt et al. 2000).

According to the Unified Model for AGN (e.g. Antonucci 1993; Urry & Padovani 1995), the Narrow Line Region (NLR) is expected to present a bi-conical shape, within which gas outflows due to

* E-mail: gabrieleilha1994@gmail.com

winds from the accretion disk are expected to be observed. However, Hubble Space Telescope (HST) narrow-band [O III] λ 5007 images of a sample of 60 nearby Seyfert galaxies show that the bi-conical shape of the NLR is not as common as expected (Schmitt et al. 2003) and gas outflows are seen only in 33% of Seyfert galaxies, as revealed by long-slit spectroscopy of 48 nearby AGN (Fischer et al. 2013). Nevertheless, long-slit observations are restricted to only one position angle. A better mapping of the outflows and their geometries can be obtained via integral field spectroscopy (IFS), as shown in recent studies both in the optical and near-infrared (e.g. Lena et al. 2015; Schnorr-Müller et al. 2014; Zakamska et al. 2016; Riffel et al. 2014; Barbosa et al. 2014).

The comparison between the gas and stellar kinematics on kiloparsec scales allows the study of the possible impact of AGN outflows on its host galaxy. So far, most studies aimed to investigate gas outflows from AGN have been performed for small samples or individual galaxies. In this work we use the observations from the Mapping Nearby Galaxies at the Apache Point Observatory (MaNGA) survey (Bundy et al. 2015) to compare the gas and stellar kinematics of a sample composed by 62 AGN observed in the MPL-5 (MaNGA Product Launch V) (Data Release 14, Abolfathi et al. 2018) with those of a control sample of inactive galaxies, matched with the AGN sample by properties of the host galaxies. If an AGN sample presents strong outflows, the large-scale gas velocity fields are expected to be disturbed when compared to the stellar velocity fields, while for inactive galaxies, the stellar and gas velocity fields are expected to be similar. Another way that AGN can affect the gas dynamics is by increasing the gas velocity dispersion due to the shocks of the nuclear outflow with the ambient gas.

The AGN and control samples used in this paper are described in Rembold et al. (2017) (hereafter Paper I), which presents also the study of the nuclear stellar populations. This is the third paper of a series aimed to compare properties of AGN hosts and their control galaxies. Besides Paper I, the spatially resolved stellar populations is investigated in Mallmann et al. (2018) (Paper II). In addition, the gas excitation and distribution will presented by Nascimento et al. (in preparation – Paper IV).

This paper is organized as follows: Section 2 presents the samples of active and inactive galaxies and the data analysis methods, while Section 3 presents the results, which are discussed in Section 4. Finally, the conclusions of this work are presented in Section 5.

2 THE DATA AND ANALYSIS

2.1 Sample and MaNGA data

We use the datacubes obtained within the MaNGA survey of the sample of AGN and matched control sample defined in Paper I. The MaNGA survey is part of the fourth-generation Sloan Digital Sky Survey (SDSS-IV) and is aimed to observe $\sim 10,000$ nearby galaxies using optical Integral Field Spectroscopy (IFS) covering the spectral range 3600–10000 Å and spectral resolving power $R \sim 2000$ at a spatial resolution of 1–2 kpc. The MaNGA sample of galaxies was designed to cover at least $1.5 R_e$ (R_e – effective radius). Here the effective radius is defined as the radius that contains the half luminosity of galaxy measured at the i-band as described in Bundy et al. (2015). The MaNGA survey science goals are presented in Bundy et al. (2015), the design and performance of the Integral Field Units are discussed in Drory et al. (2015) and the MaNGA sample is presented in Wake et al. (2017). Yan et al.

(2016b) present the survey design, execution, and data quality, the observing strategy is presented in Law et al. (2015) and the data reduction and calibrations are discussed in Law et al. (2016) and Yan et al. (2016a).

Our sample is composed by the first 62 AGN observed with MaNGA – selected from MaNGA MPL-5 (Data Release 14, Abolfathi et al. 2018). For each AGN, two control inactive galaxies, matched to the AGN hosts in absolute magnitude, galaxy mass, redshift, morphological type and inclination, were selected. The AGN selection realized by Rembold et al. (2017) is based on single-fiber SDSS-III observations. A detailed description and characterization of the AGN and control samples is presented in Paper I and the properties of AGN and control galaxies are show in Table A2 and A3, respectively. Wylezalek et al. (2018) found 173 galaxies that would not have been selected as AGN candidates based on single-fiber spectral measurements, but MaNGA allowed AGN selection based on the fully spatially resolved optical diagnostics and in the future papers similar work will be done for “nuclear” AGN and “off-nuclear” AGN. Thus, in this work we focus on the “nuclear” AGN. As mentioned in Rembold et al. (2017), our AGN sample includes 34 (55 per cent) spiral and 18 (29 per cent) elliptical galaxies. The remaining 10 objects (16 per cent) comprise 6 E/S galaxies, 1 merger and 3 unclassified objects.

2.2 Spatial filtering and noise removal

In order to remove noise from the observed datacubes, without loss of angular resolution, we performed a spatial filtering of the datacubes using a Butterworth bandpass filter (Gonzalez & Woods 2002). This filter is performed in the frequency domain. We used a low-bandpass filter to remove high spatial frequency components from the cubes, which are usually due to spurious features (e.g. bad pixels or cosmic rays). This procedure allow us to improve the fit the emission and absorption line spectra, as compared with the original datacubes.

To perform the spatial filtering, we used the Interactive Data Language (IDL) routine *bandpass_filter.pro*, which allows the choice of the cut-off frequency (ν) and the order of the filter n . A low value of n (e.g. 1) is close to a Gaussian filter, while a high value (e.g. 10) corresponds to an Ideal filter. We used $n = 5$ and $\nu = 0.25$ Ny, chosen by comparing the filtered cubes with the original ones. For lower values of ν , besides the removal of spatial noise, the filter excludes also emission from the nucleus of the galaxy.

2.3 Spectral fitting

In order to measure the emission-line fluxes and the stellar and gas kinematics from the MaNGA datacubes, we used the Gas AND Absorption Line Fitting (GANDALF) code (Sarzi et al. 2006; Oh et al. 2011). In brief, the GANDALF code fits the emission and absorption lines simultaneously, allowing the separation of the relative contribution of the stellar continuum and of nebular emission in the spectra of the galaxies. To subtract the underlying stellar contribution on the spectra of the galaxy and measure the stellar kinematics, GANDALF uses the Penalized Pixel-Fitting (PPXF) routine (Cappellari & Emsellem 2004; Cappellari 2017). The continuum spectra of the galaxy is fitted by using a library of template spectra under the assumption that the line-of-sight velocity distribution (LOSVD) of the stars is well reproduced by a Gauss-Hermite series.

As template spectra, we used 30 selected Evolutionary Pop-

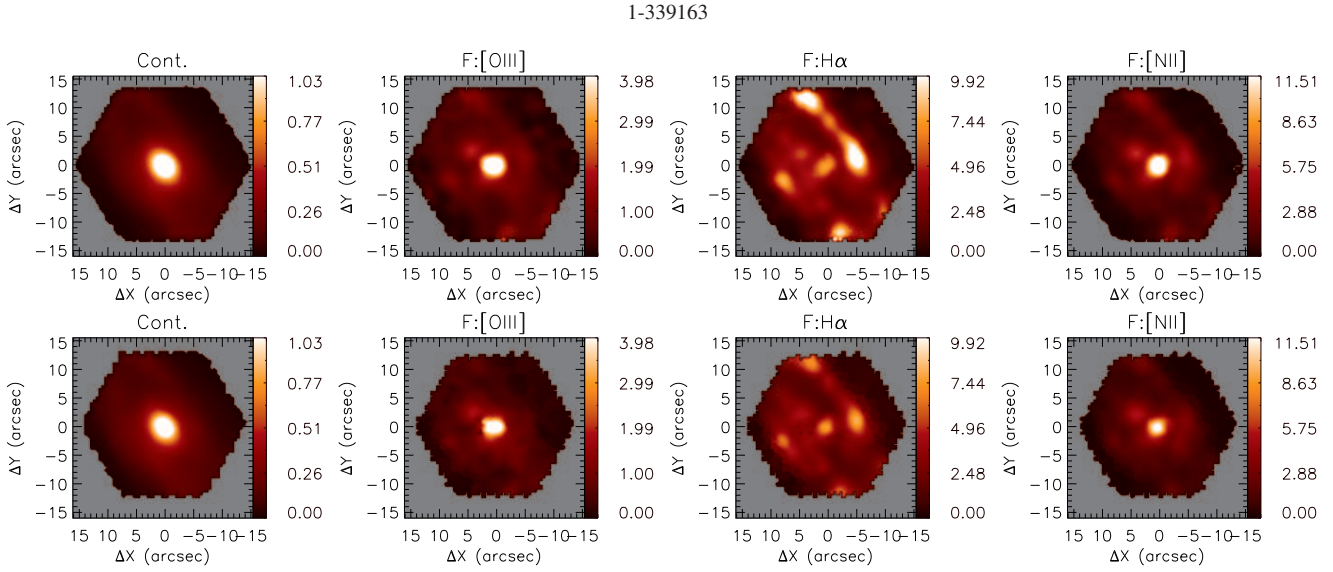


Figure 1. Emission lines fluxes for the galaxy with *mangaid* 1-339163. Our measurements are shown at the top row and the MaNGA-DAP measurements at the bottom row. In all panels, the North points up and East to the left and the x and y labels show the distance relative to the peak of the continuum emission. The first column shows a map of the continuum emission obtained by collapsing the whole spectral range, the following columns exhibit the spatial distribution of the emission line fluxes for [O III]5007 Å, H α and [N II]6583 Å, respectively. The color bars show the fluxes in unit of $10^{-17} \text{ erg s}^{-1} \text{ cm}^{-2} \text{ spx}^{-1}$.

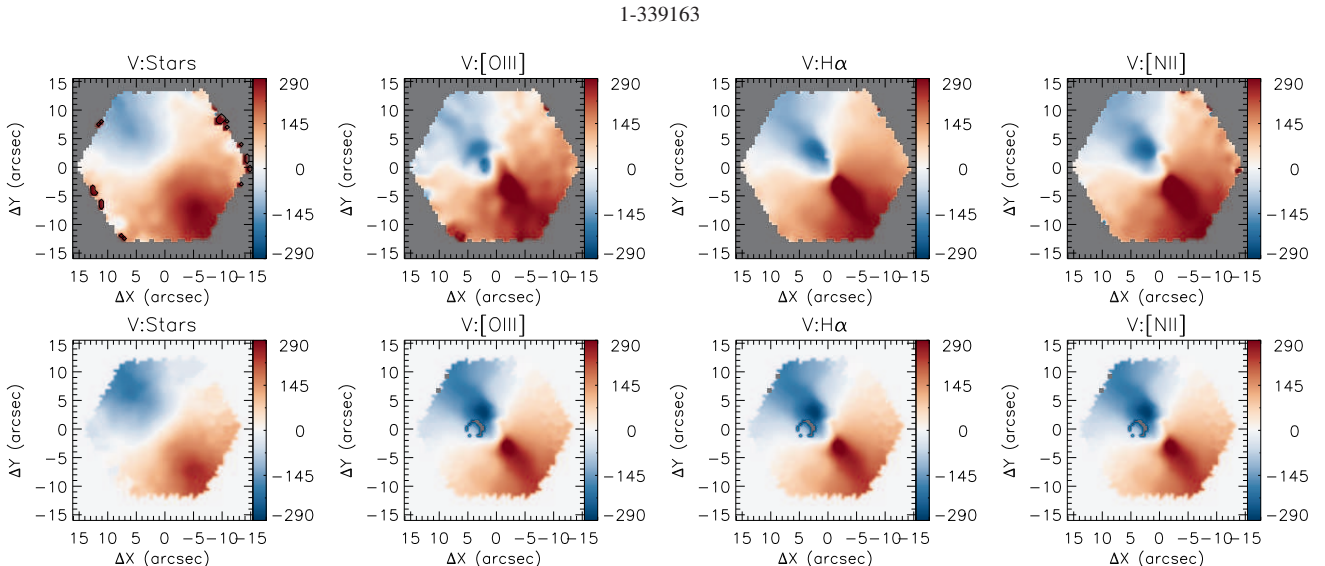


Figure 2. Velocity fields for the galaxy *mangaid* 1-339163. Our measurements are shown at the top row and the DAP measurements at the bottom row. In all panels, the North points up and East to the left and the x and y labels show the distance relative to the peak of the continuum emission. The systemic velocity has been subtracted from each panel. The first column shows the stellar velocity field and the following columns exhibit the velocity fields for [O III], H α and [N II], respectively. The velocity maps are in unit of km s^{-1} relative to the systemic velocity of the galaxy.

ulation Synthesis models from [Bruzual & Charlot \(2003\)](#), covering ages ranging from 5 Myr to 12 Gyr and three metallicities ($0.004 Z_{\odot}, 0.02 Z_{\odot}, 0.05 Z_{\odot}$). During the fit of the spectra, we allowed the use of an order 3 multiplicative Legendre polynomial to correct the shape of the continuum and only the first two Gauss-Hermite moments (velocity and velocity dispersion) were included to represent the LOSVD. We have tested the inclusion of higher order moments, but achieved the best results in the fitting process by considering only the first and second moments.

The emission-line profiles were fitted by Gaussian curves, by keeping tied the centroid velocity and width of the

[N II] $\lambda\lambda 6548, 6583$ and [S II] $\lambda\lambda 6716, 6731$ emission lines, fitting each doublet separately. In addition, the following line flux-ratio was kept fixed to their theoretical value: $[\text{N II}]\lambda 6583/[\text{N II}]\lambda 6548 = 2.94$ ([Osterbrock & Ferland 2006](#)). GANDALF gives as output measurements for the centroid velocity and velocity dispersion (σ) of the stars, and the flux, centroid velocity and σ of the emission lines for each spaxel, used to construct two-dimensional maps.

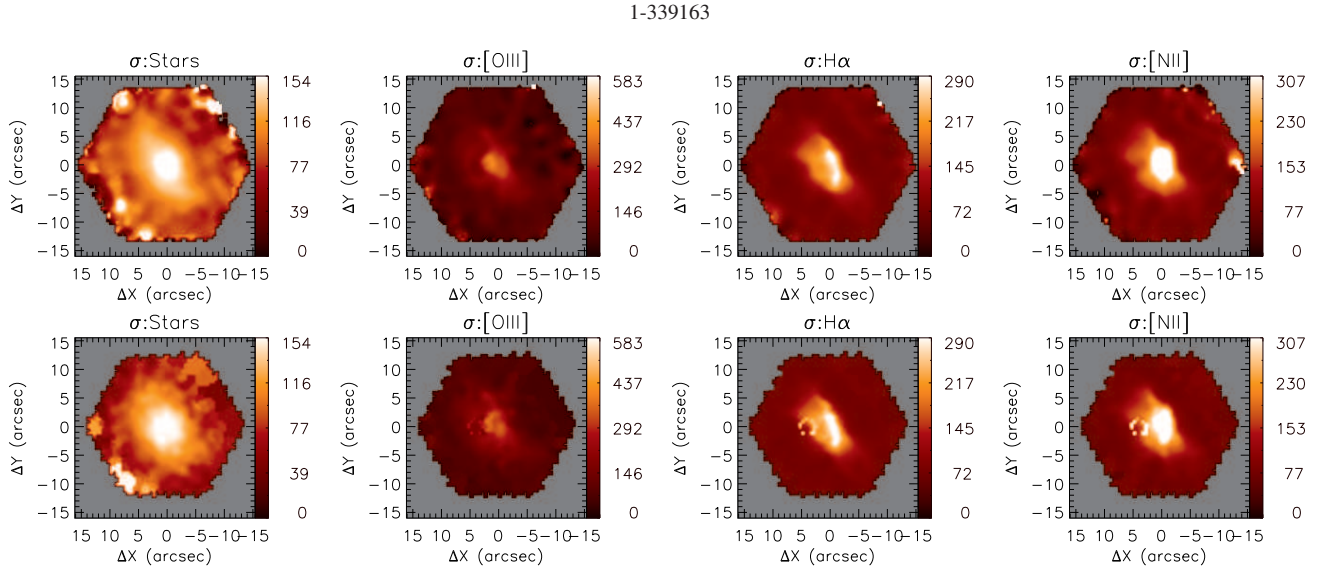


Figure 3. Velocity dispersion maps for the galaxy with *mangaid* 1-339163. Our measurements are shown at the top row and the DAP measurements at the bottom row. In all panels, the North points up and East to the left and the x and y labels show the distance relative to the peak of the continuum emission. The first column shows the stellar velocity dispersion distribution and the following columns exhibit the gas velocity dispersion distributions for [O III], H α and [N II], respectively. The color bars show the velocity dispersion corrected by instrumental broadening in units of km s^{-1} .

2.4 Measurements of the Kinematic Position Angles

In order to measure the global kinematic PA (i.e. the orientation of line of nodes – Ψ_0) from the stellar and gas velocity fields we used the kinemetry method (Krajnović et al. 2005). This method extracts general kinematic properties of the galaxies by the symmetrization of the observed velocity fields, without the need of any assumption on the geometry of the stellar distribution. To obtain the global kinematic PA, the kinemetry method performs the symmetrization of the observed velocity fields. In this process for each possible PA it is created a symmetric velocity field $V'(x, y)$, with the PA oriented along the x axis. The symmetric velocity field is obtained by changing the mean velocity of each bin for the weighted average of the corresponding velocity in the four quadrants of the velocity field. The global kinematic PA is the one that minimizes $\chi^2 = \sum_{n=1}^N (V'(x, y) - V(x, y)/\Delta V)^2$, where $V(x, y)$ is the value of observed velocity field at the position (x, y) .

We used the IDL routine *fit_kinematic_pa.pro*¹, which is an implementation of the kinemetry method and allows the measurement of the global kinematic PA and systemic velocity of the galaxy from the observed velocity fields. The routine is an implementation of the method presented in Appendix C of Krajnović et al. (2006) and has been used to study the stellar kinematics of large samples of galaxies, as for example the SAURON (Cappellari et al. 2007) and ATLAS^{3D} (Krajnović et al. 2011) surveys.

3 RESULTS

We have performed measurements for the stellar and gas kinematics and emission-line fluxes for H β , [O III] $\lambda 5007$, H α , [N II] $\lambda\lambda 6549, 83$ and [S II] $\lambda\lambda 6716, 31$. With the aim of testing our measurements, we have compared the emission-line fluxes, centroid velocities and velocity dispersions with measurements provided by the MaNGA

Data Analysis Pipeline (DAP – Westfall K. B., in prep.), as part of the MPL-7.

Figure 1 shows an example of our measurements (top row) compared with those from the DAP (bottom row) for the AGN *mangaid* 1-339163. The first column shows a map of the continuum emission, the following columns exhibit maps of emission line fluxes for [O III] $\lambda 5007$ Å, H α and [N II] $\lambda 6583$ Å, respectively. The comparison between the top and bottom rows show that our flux measurements are similar to those provided by the DAP.

In Figure 2 we show the velocity fields for the same galaxy *mangaid* 1-339163. We present the stellar velocity field together with the gas velocity fields derived for the same emission lines presented in Fig. 1. For comparison, we show our results in the top row while the results from DAP are shown in the bottom row. The comparison show that the two velocity fields are similar, although the DAP maps are noisier.

The comparison of the velocity dispersion maps obtained by us and from the DAP is shown in Figure 3, following the same pattern of organization as the previous figures. As for the centroid velocity and emission-line flux maps, the σ maps from DAP are noisier than ours. The gas and stellar σ values will be used to search for outflows in the central region of the galaxies of our sample.

As noticed in Figs 1–3, our measurements are in general consistent with those provided by DAP, but the spatial filtering of the data allows the exclusion of spurious data, as clearly seen in the maps for the [N II] $\lambda 6583$ Å and H α velocity dispersion, for which the maps constructed using the DAP shows a spurious feature at 4'' east of the nucleus, which is not present in our measurements. On the other hand, the DAP has the advantage of providing measurements for all emission lines present in the galaxy spectra, while we fit only the strongest lines. However, a detailed comparison of our measurements and those provided by DAP is beyond the scope of this paper.

In order to verify if outflows of gas from the central AGN affects significantly the kinematics of AGN hosts, we can compare the kinematic position angle (Ψ_0) of the gas and stellar velocity fields.

¹ This routine was developed by M. Cappellari and is available at <http://www-astro.physics.ox.ac.uk/~mxc/software>

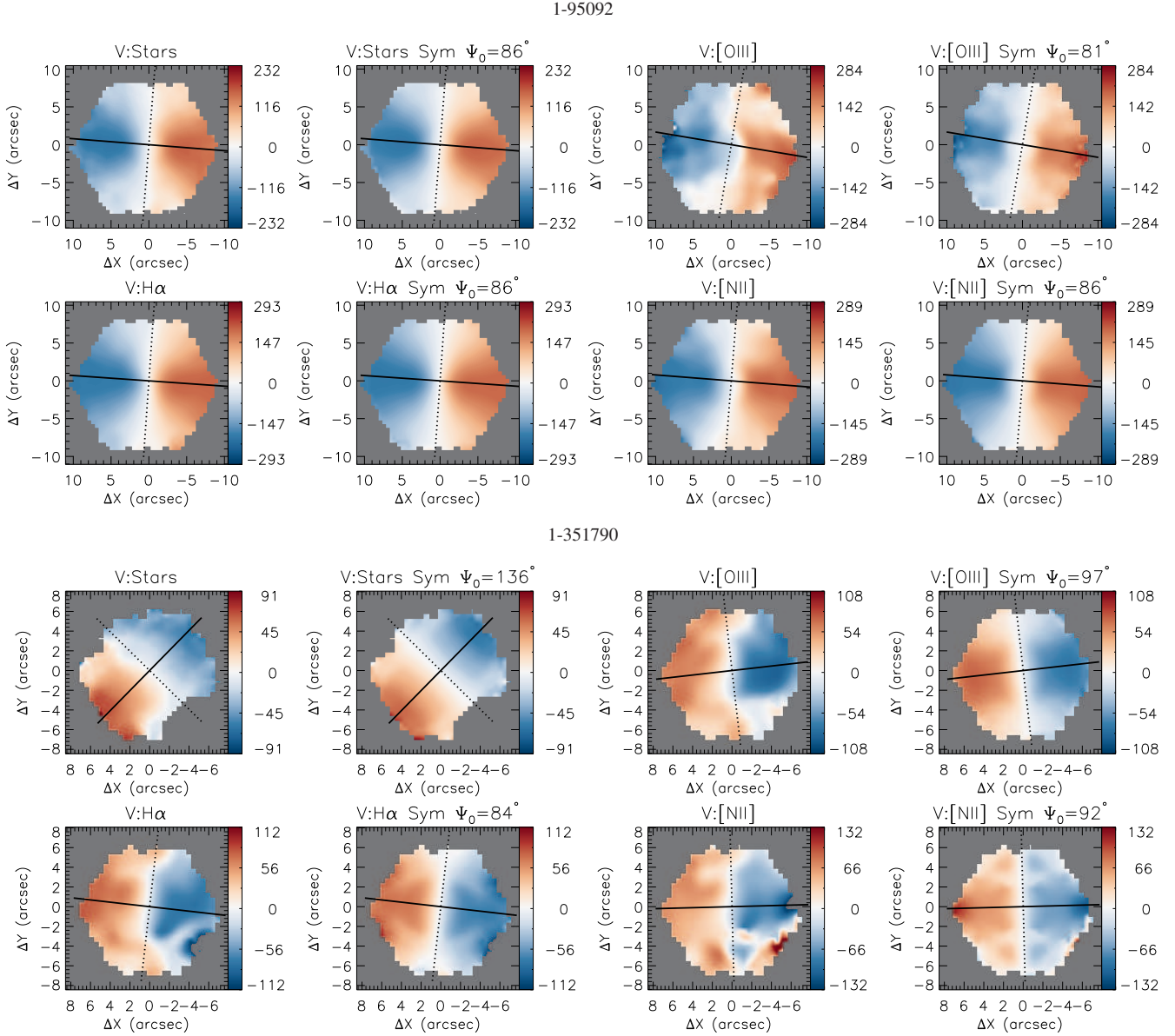


Figure 4. In the first two rows we show the derived velocity fields for the AGN *mangaid* 1-95092. The first row shows, from left to right, the stellar velocity field (V:Stars), the symmetrized stellar velocity field (V:Stars Sym), the gas velocity field for [O III] (V:[OIII]), and the corresponding symmetrized velocity field (V:[OIII] Sym). The second row shows, from left to right, the H α velocity field (V:H α), its symmetrized velocity field (V:H α Sym), the velocity and symmetrized velocity fields for [N II] (V:[NII]) and (V:[NII] Sym), respectively. In the bottom two rows we show the same velocity maps but for the AGN *mangaid* 1-351790. In all velocity maps the solid black line shows the position angle of kinematic major axis, the value of the Ψ_0 is shown in the top right-corner of the symmetrized velocity maps. The continuous (dotted) line shows the orientation of the kinematic major (minor) axis of the galaxy. The color bars show the velocities in units of km s $^{-1}$.

The motion of the stars is dictated by the gravitational potential of the galaxy, while for the gas, an additional component due to outflows is expected for the AGN. By comparing the difference between the Ψ_0 values derived from the gas and stellar velocity fields for AGN and control samples, one should expect larger differences for the AGN if strong outflows are present.

We derived Ψ_0 for the stellar and gas velocity fields using [O III]5007 Å, H α and [N II]6583 Å emission lines. In Figure 4 we show two examples of the observed and symmetrized velocity fields for two AGN (*mangaid* 1-95092 and *mangaid* 1-351790). This figure illustrates two distinct results: (i) the Ψ_0 from distinct emission-line velocity fields are very similar to each other for both galaxies; (ii) for

the galaxy *mangaid* 1-95092 the Ψ_0 derived from the stellar velocity field is very similar to that derived for the gas velocity field. (iii) in the case of the AGN host *mangaid* 1-351790 the orientation of the kinematic major axis of the stellar and gas velocity fields show a significant offset. In Figure 5 we show a similar figure for two control galaxies: *mangaid* 12-129446 and *mangaid* 1-178838, showing similar results as those observed for the AGN: similar Ψ_0 for all emission lines and in one case a distinct Ψ_0 for the gas and stars. From Fig. 4 and Fig. 5 we can conclude that for this galaxies both AGN and controls present a rotation pattern in the stellar as well as in the gas velocity fields. In Table A1 we present the kinematic position angle derived for all galaxies of our sample.

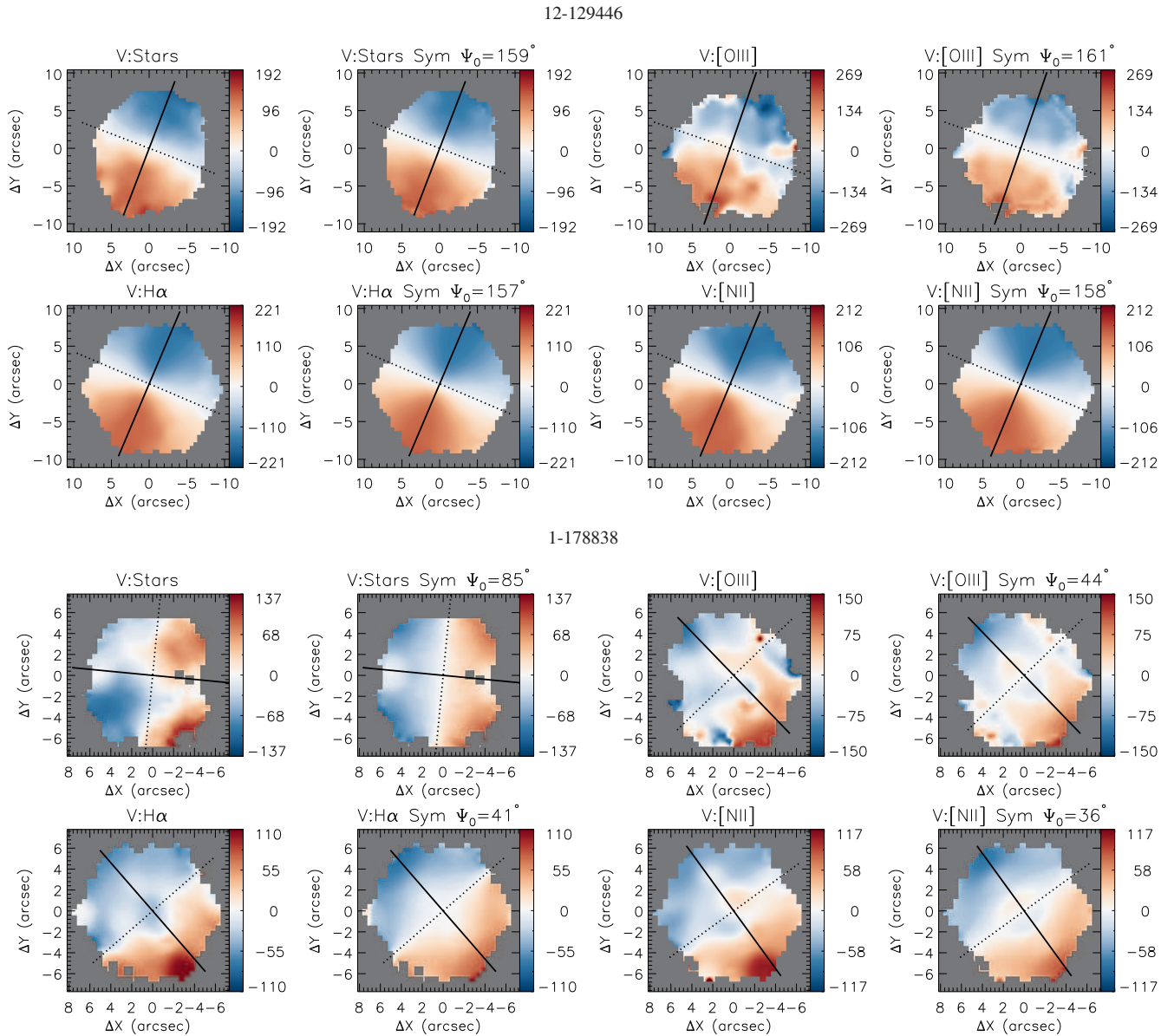


Figure 5. Same as Fig. 4 for the control galaxies *mangaid* 12-129446 (first and second row) and *mangaid* 1-178838 (third and fourth row). The velocity fields are in unit of km s^{-1} .

4 DISCUSSION

In order to investigate if the AGN feedback in our sample is powerful enough to disturb the gas kinematics on galactic scales and change the orientation of the kinematic major axis of the galaxy, we calculated the frequency of occurrence of a given PA offset in the AGN and control samples. We computed the difference in the PA offset in the $\Psi_{0\star}$ of the stellar velocity field with respect to the $\Psi_{0\text{gas}}$ derived for [O III]5007 Å, H α and [N II]6583 Å emission-line velocity fields. The resulting histograms of the PA offsets ($\Delta\text{PA} = |\Psi_{0\text{gas}} - \Psi_{0\star}|$) are presented in Figure 6. The top panels show the results using the [O III] velocity fields, while the middle panel show these results for H α and the bottom panel for [N II]. AGN are represented by blue colors and control galaxies are shown red.

We find no clear difference in the distribution of ΔPA for the AGN and control samples. Similar values of ΔPA are observed for distinct emission lines. Although a few galaxies display large ΔPA .

values, for most of them ΔPA is smaller than 30° . For 79 % of AGN and 81 % of control galaxies the PA offsets are smaller than 30° as measured using the [O III]5007 Å velocity field as representative of the gas velocity field. This result indicates that the AGN feedback is not strong enough to disturb – more than in a control sample – the gas kinematics on the galactic scales probed by MaNGA. Indeed, the sample of active galaxies used here is composed mainly by low-luminosity AGN (Rembold et al. 2017), for which outflows from the accretion disk are expected to be weak and thus the gas velocity fields of these AGN hosts on galactic scales are expected to be driven by the gravitational potential of the galaxy. Besides that, Wylezalek et al. (2017) only find evidence for an AGN-driven outflow in a MaNGA-selected AGN candidate when zoom into the center with higher spatial resolution. The resolution of MaNGA is only $1''.5$ – $2''.5$, so a lot of small scale outflows may be hidden. We do not find any clear difference in the ΔPA of high and low luminosity AGN.

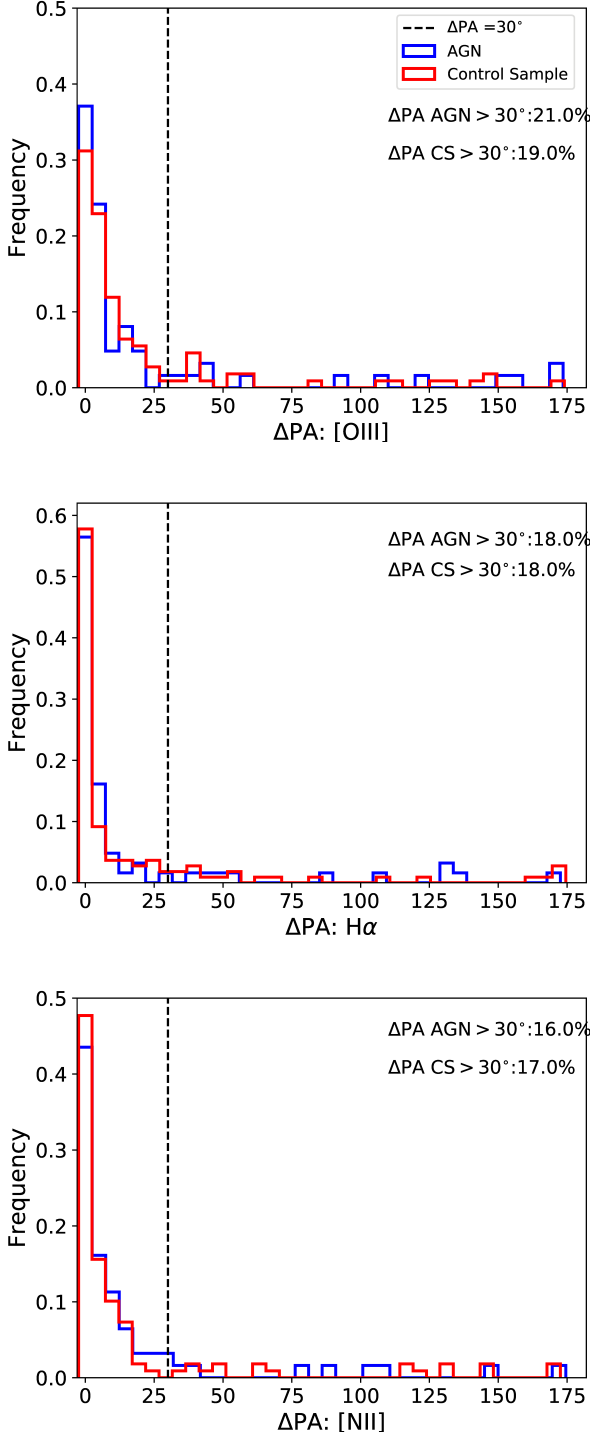


Figure 6. Histograms comparing ΔPA distributions of AGN and control galaxies for $[O\text{ III}]\lambda 5007$ (top panel), $H\alpha$ (middle panel) and $[N\text{ II}]\lambda 6583$ (bottom panel). AGN are shown in blue and controls in red. The vertical dashed lines show $\Delta PA=30^\circ$.

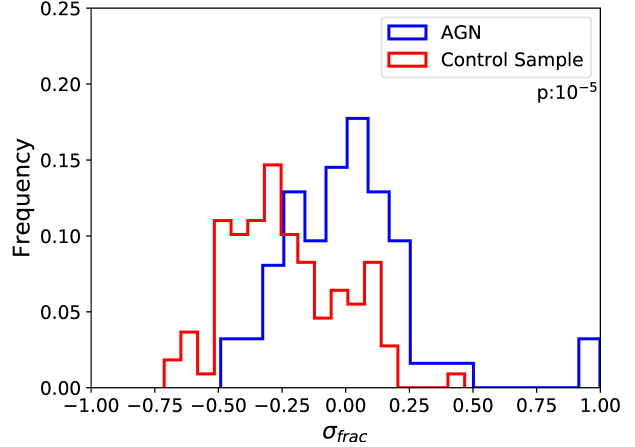


Figure 7. Histograms comparing σ_{frac} distributions of AGN and control galaxies for $[O\text{ III}]\lambda 5007$. AGN are shown in blue and controls in red. The result of Anderson-Darling statistical test returns a p-value of 10^{-5} , confirming that AGN and inactive galaxies follow distinct distributions in σ_{frac} .

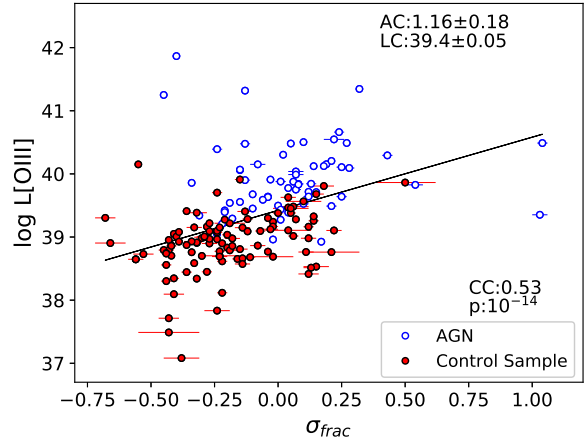


Figure 8. Plot of logarithm of $[O\text{ III}]\lambda 5007$ Å luminosity versus σ_{frac} for AGN (blue open circles) and inactive galaxies (red closed circles). The Spearman test confirms that these properties are correlated resulting in a correlation coefficient of 0.53 and p-value of 10^{-14} . The black line is the result of linear fit of data, with linear coefficient of $LC = 39.4 \pm 0.05$ and angular coefficient of $AC = 1.16 \pm 0.18$.

Penny et al. (2018) analyzed low-mass galaxies ($M_\star \lesssim 5 \times 10^9 M_\odot$) of the SDSS-IV MaNGA and found that five galaxies of their sample of 13 possible dwarf AGN host, exhibit ionized gas components in $H\alpha$ that are kinematically offset from their stellar velocity field and these objects have AGN-like emission line ratios at their centers. This fact has been interpreted as due to a recent accretion episode or outflow. Furthermore, Penny et al. (2018) suggest that AGN feedback may play an important role in these low-mass galaxies. Their sample can be considered an analogous of the “Red Geysers” galaxies reported by Cheung et al. (2016) using MaNGA data. These galaxies do not show recent star formation activity, most of them harbor very low luminosity AGN, showing

large scale bi-polar outflows in ionized gas and interpreted as being originated by centrally driven winds due to a Radiatively Inefficient Accretion Flow onto the Supermassive Black Hole. These galaxies show stellar and gas kinematic major axes misaligned and account for 10% of the population of galaxies with masses of the order of $2 \times 10^{10} M_{\odot}$ that do not show recent star formation episodes. Although some galaxies of our sample show $\Delta PA > 30^\circ$, as seen in Fig. 6, the fraction of AGN and control galaxies with significant PA offset are similar (21 % and 19 % for AGN and control sample, respectively), suggesting that these offsets are not associated to the presence AGN and probably they are just statistical fluctuations. Thus, we show that standard AGN do not follow the same behavior of “Red Geyser” galaxies analyzed by Cheung et al. (2016) and the low-mass galaxies presented in Penny et al. (2018), as we do not detect significant PA offsets.

The fact that there are no significant PA offsets in our sample does not necessarily mean that the AGN do not show outflows, although it implies they do not play an important role in the galaxy scale gas kinematics. However, AGN driven outflows could be seen on smaller scales.

In order to search for signatures of outflows closer to the nuclei of the galaxies, we have compared the stellar and gas velocity dispersion values within the inner $2''.5$ diameter of the galaxies of our sample, as this aperture corresponds to the angular resolution of the MaNGA datacubes. In Table A1 we show these velocity dispersion values. On average, the $2''.5$ aperture corresponds to a physical scale of ~ 2 kpc at the typical redshift of the sample galaxies. In order to quantify the differences between the stellar and gas velocity dispersions measured in the central regions we calculated the parameter σ_{frac} , defined as:

$$\sigma_{\text{frac}} = \frac{\sigma_{\text{gas}} - \sigma_{\star}}{\sigma_{\star}}, \quad (1)$$

which measures the fractional difference between the gas and stellar velocity dispersion, and thus higher values of σ_{frac} are indicative of a disturbed kinematics (not only due to the gravitational potential of the galaxy) and most probably due to outflows.

We see a trend of AGN having generally higher σ_{frac} values than inactive galaxies as can be seen in the distributions shown in Figure 7. The median values of σ_{frac} for AGN and control sample are $<\sigma_{\text{frac}}>_{\text{AGN}} = 0.04$ and $<\sigma_{\text{frac}}>_{\text{CTR}} = -0.23$, respectively. Besides that, we note that 90% of AGN have σ_{frac} larger than -0.22 and 75% of them have values larger than -0.13 . For the control sample, 90% of the galaxies show $\sigma_{\text{frac}} < 0.12$ and for 75% of the sample $\sigma_{\text{frac}} < -0.04$. The result of the Anderson-Darling statistical test returns a p-value of 10^{-5} , that confirms that the AGN and inactive galaxies follow distinct distributions in σ_{frac} . We thus conclude that the parameter σ_{frac} can be used as an indicative of AGN activity.

We derived the luminosity of the [OIII] $\lambda 5007\text{\AA}$ emission line ($L_{[\text{O}III]}$) of each galaxy (Table A1) using the flux measurements obtained with the GANDALF code within the same aperture used to measure the σ_{frac} , and then investigated a possible correlation between σ_{frac} and $L_{[\text{O}III]}$. Figure 8 shows the plot of $L_{[\text{O}III]}$ vs. σ_{frac} for the AGN and control samples. There is a clear positive correlation between σ_{frac} and $L_{[\text{O}III]}$, with a Spearman correlation coefficient of 0.53 and a p-value of 10^{-14} . However, it should be noticed that the observed correlation could be artificially produced, as the AGN and inactive galaxies clearly show distinct distributions in σ_{frac} (Fig. 7). The Spermann test returns a p-value of 0.06 for the AGN sample and 10^{-5} for the control sample, meaning that no strong correlation is found between the $L_{[\text{O}III]}$ and σ_{frac} for the AGN

sample alone, while these parameters are correlated for the control sample. The absence of correlation for the AGN sample may be due to the fact that our sample covers only a small range of luminosities, as most objects are low-luminosity AGN (Rembold et al. 2017). Fig. 7 shows a trend of AGN having higher σ_{frac} values than inactive galaxies. The same trend can also be observed in Fig. 8. This result can be interpreted as the higher values seen for AGN as compared to control galaxies being due to winds originated in the AGN. Thus, although the AGN of the sample do not show powerful outflows that can affect the gas kinematics on galactic scales, they do show small scale outflows (within the inner 1-2 kpc).

Our results can be compared with those obtained from single aperture spectra. For example, Woo et al. (2017) find that there is a trend of the [OIII] $\lambda 5007\text{\AA}$ velocity dispersion to increase with the increase of the AGN luminosity in a sample of $\sim 110,000$ AGN and star-forming (SF) galaxies at $z < 0.3$. This trend is also present in composite objects and is not clear for star-forming galaxies. They interpreted this result as due to strong gas outflows in high luminosity AGN, indicating that AGN energetics are driving these outflows. They find also lower average [OIII] velocity dispersion values for star-forming galaxies. Our result is in good agreement with theirs. In addition, optical observations (Wylezalek et al. 2016), radio observations (Zakamska & Greene 2014) and molecular gas (Veilleux et al. 2013) as well as theoretical models (Zubovas & King 2012b) have suggested that the AGN needs to have enough luminosity for the gas to be pushed out of the galactic potential. This is in agreement with our results, where we see a positive correlation between σ_{frac} and luminosity.

5 CONCLUSIONS

We have mapped the gas and stellar kinematics of a sample of 62 AGN and 109 control galaxies (inactive galaxies) in order to investigate the effect of the AGN in the large and small scale gas kinematics of the AGN host galaxies. We detect evidence of nuclear gas outflows in the 62 AGN, but conclude they are not powerful enough to play an important role in the gas kinematics on galactic scales. The main conclusions of our work are:

- There is no significant difference in the ΔPA between active and inactive galaxies, indicating that the galaxy scale gas kinematics is dominated by orbital motion in the gravitational potential of the galaxies, instead of outflows driven by the central AGN.
- We found that the difference between the orientation of the kinematic major axes of the gas and stars (ΔPA) is larger than 30° for 13 (21 %) AGN and 21 control galaxies (19 %) using the [OIII] $\lambda 5007\text{\AA}$ kinematics.
- The AGN show larger fractional differences in the velocity dispersions of the gas and stars $\sigma_{\text{frac}} = \frac{\sigma_{\text{gas}} - \sigma_{\star}}{\sigma_{\star}}$ than inactive galaxies within the inner $2''.5$ diameter, that corresponds to 1-2 kpc at the galaxies. The mean values are $\sigma_{\text{frac}}=0.05$ for the AGN and $\sigma_{\text{frac}}=-0.23$ for the control sample. This difference is interpreted as being due to outflows from the active nuclei. This indicates that, although the AGN of our sample do not affect the gas kinematics on large scale, it does affect it at least within the inner kpc.
- A correlation between the [OIII] $\lambda 5007\text{\AA}$ luminosity and σ_{frac} is observed when putting together the AGN and control samples.

ACKNOWLEDGEMENTS

Funding for the Sloan Digital Sky Survey IV has been provided by the Alfred P. Sloan Foundation and the Participating Institutions. SDSS-IV acknowledges support and resources from the Center for High-Performance Computing at the University of Utah. The SDSS web site is www.sdss.org. SDSS-IV is managed by the Astrophysical Research Consortium for the Participating Institutions of the SDSS Collaboration including the Brazilian Participation Group, the Carnegie Institution for Science, Carnegie Mellon University, the Chilean Participation Group, Harvard-Smithsonian Center for Astrophysics, Instituto de Astrofísica de Canarias, The Johns Hopkins University, Kavli Institute for the Physics and Mathematics of the Universe (IPMU) / University of Tokyo, Lawrence Berkeley National Laboratory, Leibniz Institut für Astrophysik Potsdam (AIP), Max-Planck-Institut für Astrophysik (MPA Garching), Max-Planck-Institut für Extraterrestrische Physik (MPE), Max-Planck-Institut für Astronomie (MPIA Heidelberg), National Astronomical Observatory of China, New Mexico State University, New York University, The Ohio State University, Pennsylvania State University, Shanghai Astronomical Observatory, United Kingdom Participation Group, Universidad Nacional Autónoma de México, University of Arizona, University of Colorado Boulder, University of Portsmouth, University of Utah, University of Washington, University of Wisconsin, Vanderbilt University, and Yale University. We thank the support of the Instituto Nacional de Ciência e Tecnologia (INCT) e-Universo (CNPq grant 465376/2014-2).

This study was financed in part by the Coordenação de Aperfeiçoamento de Pessoal de Nível Superior - Brasil (CAPES) - Finance Code 001, Conselho Nacional de Desenvolvimento Científico e Tecnológico (CNPq) and Fundação de Amparo à pesquisa do Estado do RS (FAPERGS).

REFERENCES

- Abolfathi, B. et al. ApJS, 2018, 235, 42
 Antonucci, R., 1993, ARAA, 31, 473
 Bower, R. G. et al. 2006, MNRAS, 370, 645
 Barbosa, F. K. B., Storchi-Bergmann, T., McGregor, P., Vale, T. B., Riffel, R. A., 2014, MNRAS, 445, 2353
 Bundy, K., et al., 2015, ApJ 798, 7
 Bruzual G., Charlot S., 2003, MNRAS, 344, 1000
 Cappellari, M., Emsellem, E., 2004, PASP, 116, 138
 Cappellari, M. et al., 2007, MNRAS, 379, 418
 Cappellari, M., 2017, MNRAS, 466, 798
 Cheung, E., et al., 2016, Nature, 533, 504.
 Conroy, C., Gunn, J. E., White, M., 2009, ApJ, 699, 486
 Di Matteo, T., Springel, V. & Hernquist, L. 2005, Nature, 433, 604
 Drory, N., et al. 2015, AJ, 149, 77
 Ferrarese, L. & Merritt, D. A., 2000, ApJL, 539, L9
 Fischer, T. C., Crenshaw, D. M., Kraemer, S. B., Schmitt, H. R. 2013, ApJS, 209, 1
 Gebhardt, K. et al. 2000, ApJL, 539, L13
 Gonzalez R.C., Woods R.E., 2002, Digital Image Processing, 2nd edition, Prentice-Hall, Englewood Cliffs, NJ
 Hopkins, P. et al. 2005, ApJ, 630, 705
 Krajnović, D., Cappellari, M., Emsellem, E., McDermid, R. M., de Zeeuw, P. T., 2005, 357, 1113
 Krajnović, D., Cappellari, M., de Zeeuw, P. T., Copin, Y., 2006, MNRAS, 366, 787.
 Krajnović, D. et al., 2011, MNRAS, 414, 2993
 Law, D. R., et al., 2015, AJ, 150, 19
 Law, D. R., et al., 2015, AJ, 152, 83
 Lena, D. et al., 2015, ApJ, 806, 84
 Mallmann, N. D. et al. 2018, MNRAS, submitted
 Nemmen R., Bower, R., Babul, A. & Storchi-Bergmann, T. 2007, MNRAS, 377, 1652
 Oh, K., Sarzi, M., Schawinski, K., Yi, S. K., 2011, ApJS, 195, 130
 Osterbrock, D. E., & Ferland, G. J. 2006, Astrophysics of Gaseous Nebulae and Active Galactic Nuclei, 2nd ed., University Science Books, Sausalito, California
 Penny, S. J. et al. 2018, MNRAS, submitted
 Rembold, S. B. et al. 2017, MNRAS, 472, 4382
 Riffel, R. A., Storchi-Bergmann, T., Riffel, R., 2014, ApJ, 780, 24
 Sarzi, M., et al. 2006, MNRAS, 366, 1151
 Scannapieco, E. et al. 2005, ApJ, 635, L13
 Schmitt, H. R., Donley, J. L., Antonucci, R. R. J., Hutchings, J. B., Kinney, A. L., 2003, ApJS, 148, 327
 Schnorr-Müller, A., Storchi-Bergmann, T., Nagar, N. M., Robinson, A., Lena, D., Riffel, R. A., Couto, G. S., 2014, MNRAS, 437, 1708
 Springel, V., Di Matteo, T. & Hernquist, L. 2005, ApJ, 620, L79
 Tremaine, S. et al. 2002, ApJ, 574, 740
 Urry, C. M., Padovani, P., 1995, PASP, 107, 803
 Veilleux S., et al., 2013, ApJ, 776, 27
 Wake, D. A. et al., 2017, AJ, 154, 86
 Woo, J., et al., 2017, ApJ, 839, 120
 Wylezalek, D. et al. 2018, MNRAS, 474, 1499
 Wylezalek, D. et al. 2017, MNRAS, 467, 2612
 Wylezalek, D. et al. 2016, MNRAS, 461, 3724
 Yan, R., et al., 2016a, AJ, 151, 8
 Yan, R., et al., 2016b, AJ, 152, 197
 Zakamska, N. L. et al. 2016, MNRAS, 459, 3144
 Zakamska N. L., Greene J. E., 2014, MNRAS, 442, 784
 Zubovas K., King A., 2012b, ApJ, 745, L34

APPENDIX A: KINEMATIC MEASUREMENTS OF THE AGN AND CONTROL SAMPLES

Table A1. Kinematic measurements of the AGN and control samples. Col. 1: *mangaid*; Col. 2: Logarithm of luminosity of [O III]5007 Å in erg s⁻¹ within the inner 2''.5 diameter; velocity dispersion in km s⁻¹ obtained for stars, [O III]5007 Å, H α , [N II]6583 Å (cols. 3-6), measured within the inner 2''.5 diameter, and kinematic position angles (Ψ_0) for the stars, [O III]5007 Å, H α , [N II]6583 Å (cols. 7-10). In each block we have the parameters obtained for AGN (first line) and their controls (second and third lines).

<i>mangaid</i>	$\log_{10} L_{[O\,III]}$	σ_\star	$\sigma_{[O\,III]}$	$\sigma_{H\alpha}$	$\sigma_{[N\,II]}$	$\Psi_0 \star$	Ψ_0 [O III]	Ψ_0 H α	Ψ_0 [N II]
1-558912	41.32	269.0±3.0	231.0±1.0	204.0±2.0	209.0±2.0	148.0±0.5	165.0±0.5	117.5±0.5	158.5±0.5
1-71481	39.38	284.0±2.0	194.0±12.0	275.0±12.0	219.0±11.0	174.0±0.5	146.5±0.5	9.5±0.5	163.5±0.5
1-72928	39.45	253.0±1.0	268.0±19.0	161.0±20.0	295.0±126.0	138.0±0.5	134.0±0.5	121.0±0.5	137.5±0.5
1-269632	41.35	153.0±1.0	202.0±2.0	137.0±2.0	155.0±1.0	16.0±2.2	173.5±0.5	11.5±2.0	14.0±0.8
1-210700	39.7	199.0±2.0	150.0±4.0	112.0±1.0	131.0±1.0	130.0±0.5	137.5±0.5	134.5±0.5	119.5±0.5
1-378795	39.4	172.0±2.0	148.0±5.0	109.0±1.0	128.0±3.0	19.5±0.5	25.5±0.5	20.5±0.5	19.0±0.5
1-258599	41.87	349.0±3.0	208.0±1.0	170.0±1.0	166.0±1.0	81.5±0.5	98.5±0.5	122.5±0.5	108.5±0.5
1-93876	39.11	223.0±1.0	230.0±20.0	275.0±18.0	98.0±18.0	146.0±0.5	148.5±0.5	149.5±0.5	136.0±0.5
1-166691	38.76	231.0±1.0	281.0±25.0	175.0±15.0	221.0±39.0	92.0±0.5	146.5±0.5	34.5±0.5	95.0±0.5
1-72322	41.25	287.0±3.0	156.0±2.0	170.0±2.0	182.0±3.0	107.0±0.8	114.5±0.5	116.0±0.5	118.5±0.5
1-121717	39.86	223.0±2.0	334.0±26.0	167.0±3.0	173.0±4.0	134.0±0.5	111.0±0.5	134.0±0.5	134.0±0.5
1-43721	39.48	250.0±1.0	265.0±14.0	132.0±2.0	140.0±2.0	55.0±2.2	52.0±0.5	51.5±0.5	43.0±0.5
1-121532	40.55	260.0±1.0	318.0±10.0	280.0±8.0	300.0±8.0	101.0±0.5	148.5±0.5	10.0±0.5	77.0±0.5
1-218427	38.9	386.0±13.0	130.0±21.0	616.0±191.0	466.0±133.0	136.5±0.5	178.0±0.5	136.5±0.5	136.0±0.5
1-177493	39.91	172.0±2.0	145.0±2.0	156.0±3.0	111.0±2.0	142.0±3.8	145.0±2.0	158.0±0.5	149.0±0.5
1-209980	40.66	179.0±3.0	218.0±1.0	233.0±1.0	245.0±1.0	50.0±0.8	52.0±0.5	55.0±0.5	51.5±0.5
1-295095	38.76	101.0±1.0	112.0±3.0	80.0±1.0	88.0±2.0	1.0±2.2	3.0±0.8	178.0±1.5	1.0±1.2
1-92626	39.41	181.0±2.0	116.0±2.0	138.0±2.0	183.0±10.0	10.5±0.8	13.5±0.5	13.0±0.5	13.0±0.5
1-44379	40.49	133.0±2.0	168.0±2.0	126.0±3.0	159.0±3.0	15.0±0.5	14.0±0.5	16.5±0.5	16.5±0.8
1-211082	38.86	153.0±1.0	89.0±3.0	118.0±2.0	158.0±1.0	157.5±0.5	163.5±0.5	159.0±0.5	159.5±0.5
1-135371	38.9	144.0±2.0	105.0±4.0	116.0±2.0	147.0±4.0	67.5±0.8	72.5±0.5	66.5±0.8	66.5±0.5
1-149211	40.5	107.0±1.0	116.0±0.0	121.0±1.0	134.0±2.0	41.0±0.5	166.0±0.5	174.5±0.5	25.5±0.5
1-377321	40.15	182.0±6.0	77.0±0.0	77.0±0.0	80.0±0.0	17.5±0.5	26.5±0.5	44.0±0.5	85.5±0.5
1-491233	39.09	106.0±1.0	94.0±1.0	83.0±1.0	87.0±1.0	120.5±1.5	105.0±1.8	118.5±1.2	118.5±1.5
1-173958	40.49	101.0±1.0	207.0±2.0	114.0±1.0	142.0±2.0	10.0±4.2	32.0±0.5	18.5±3.2	21.0±0.5
1-247456	39.3	879.0±34.0	172.0±13.0	1090.0±327.0	749.0±91.0	149.0±1.2	169.0±0.5	167.5±0.8	167.5±0.5
1-24246	39.1	110.0±1.0	134.0±4.0	94.0±2.0	105.0±2.0	139.0±1.5	134.0±0.8	134.0±1.0	121.5±0.5
1-338922	40.39	284.0±2.0	215.0±5.0	215.0±3.0	212.0±1.0	47.5±3.8	110.5±0.5	103.0±0.5	129.5±0.5
1-286804	39.81	179.0±3.0	204.0±5.0	171.0±4.0	173.0±3.0	168.5±0.5	164.0±1.2	169.5±0.5	153.0±0.5
1-109493	39.56	257.0±2.0	278.0±17.0	521.0±140.0	215.0±8.0	102.5±0.5	42.0±0.5	58.5±0.5	137.5±0.5
1-279147	40.29	116.0±1.0	163.0±1.0	101.0±1.0	122.0±1.0	31.5±4.2	51.5±0.5	54.0±0.5	1.0±0.5
1-283246	38.68	142.0±0.0	126.0±3.0	157.0±8.0	140.0±3.0	37.0±2.8	59.0±1.0	29.5±0.5	31.0±0.5
1-351538	39.26	109.0±1.0	125.0±3.0	69.0±0.0	76.0±1.0	160.5±16.2	141.0±0.5	169.0±1.2	176.5±1.2
1-460812	40.48	210.0±3.0	179.0±2.0	212.0±1.0	218.0±3.0	78.0±0.8	78.5±0.5	69.5±0.5	68.5±0.5
1-270160	39.63	319.0±3.0	331.0±9.0	362.0±17.0	311.0±10.0	111.0±0.5	112.5±0.5	104.0±0.5	116.5±1.0
1-258455	39.15	214.0±1.0	184.0±7.0	184.0±3.0	194.0±7.0	131.0±1.5	130.0±0.5	128.5±0.5	127.5±0.5
1-92866	40.3	241.0±1.0	244.0±2.0	217.0±1.0	258.0±2.0	18.5±1.5	126.5±0.5	151.0±0.5	123.5±0.5
1-94514	38.69	237.0±1.0	229.0±18.0	373.0±71.0	386.0±23.0	147.5±1.0	147.0±0.5	143.0±0.5	135.0±0.5
1-210614	38.91	223.0±1.0	152.0±3.0	178.0±2.0	157.0±3.0	131.0±2.2	90.0±0.5	95.0±0.5	82.0±0.5
1-94784	40.48	135.0±1.0	142.0±2.0	156.0±1.0	153.0±2.0	65.5±1.0	71.0±0.5	62.5±0.8	67.5±1.5
1-211063	38.75	136.0±1.0	76.0±2.0	141.0±2.0	111.0±2.0	170.0±1.8	164.0±0.5	166.5±1.8	165.0±1.2
1-135502	39.16	164.0±1.0	117.0±1.0	177.0±2.0	163.0±1.0	98.5±0.5	98.5±0.5	101.5±0.5	102.0±0.5
1-44303	40.15	114.0±1.0	135.0±1.0	120.0±2.0	134.0±2.0	56.0±7.2	39.0±7.8	67.5±2.0	62.0±3.0
1-339028	39.22	183.0±1.0	133.0±2.0	170.0±3.0	145.0±1.0	179.5±2.7	173.5±1.0	5.5±0.8	9.0±1.8
1-379087	39.27	131.0±1.0	104.0±2.0	123.0±1.0	125.0±1.0	39.5±2.2	31.5±0.5	42.5±0.5	44.0±1.0
1-339094	40.2	133.0±1.0	160.0±1.0	152.0±2.0	157.0±2.0	0.0±1.5	176.0±1.8	175.0±0.8	8.0±0.5
1-274646	38.91	121.0±1.0	82.0±1.0	108.0±1.0	108.0±1.0	61.5±17.2	175.0±0.5	41.0±0.5	22.5±0.5
1-24099	38.34	125.0±2.0	84.0±2.0	131.0±17.0	153.0±6.0	125.5±1.2	135.5±0.8	134.5±0.5	121.5±0.5

Table A1 – continued

mangaid	$\log_{10} L_{[O\,III]}$	σ_\star	$\sigma_{[O\,III]}$	$\sigma_{H\alpha}$	$\sigma_{[N\,II]}$	$\Psi_0 \star$	Ψ_0 [O III]	Ψ_0 H α	Ψ_0 [N II]
1-137883	40.15	185.0±5.0	164.0±3.0	133.0±3.0	130.0±2.0	55.5±2.0	56.5±0.8	48.0±1.2	41.5±0.5
1-178838	38.69	114.0±2.0	90.0±5.0	107.0±3.0	103.0±2.0	84.5±1.5	44.0±0.5	41.0±4.8	36.0±2.2
1-36878	39.07	138.0±3.0	101.0±1.0	90.0±1.0	98.0±1.0	46.0±1.0	26.0±0.5	43.0±0.5	45.5±1.2
1-48116	40.12	151.0±1.0	178.0±1.0	127.0±1.0	134.0±1.0	56.0±1.0	65.0±0.5	57.0±1.0	56.0±0.5
1-386452	39.09	123.0±1.0	90.0±1.0	89.0±1.0	91.0±1.0	135.0±2.0	131.0±0.5	131.5±1.0	131.0±1.2
1-24416	38.76	157.0±1.0	104.0±1.0	162.0±3.0	148.0±2.0	85.0±0.8	79.5±0.8	83.5±0.5	82.5±0.5
1-256446	40.12	214.0±2.0	244.0±1.0	231.0±1.0	232.0±1.0	158.0±11.0	62.0±0.5	48.0±4.2	49.5±0.5
1-322671	38.7	173.0±1.0	134.0±12.0	360.0±121.0	167.0±12.0	130.0±3.2	109.0±0.5	101.5±0.5	143.0±0.5
1-256465	39.38	217.0±1.0	227.0±4.0	187.0±3.0	216.0±6.0	134.0±16.0	75.0±0.5	62.5±0.5	64.0±0.5
1-95585	40.11	171.0±1.0	214.0±3.0	211.0±3.0	206.0±2.0	69.5±1.0	62.5±0.5	68.0±0.5	69.5±0.5
1-166947	38.79	149.0±1.0	83.0±3.0	143.0±3.0	116.0±2.0	36.0±3.2	123.0±0.5	34.0±0.8	35.5±0.8
1-210593	39.04	160.0±1.0	128.0±3.0	146.0±4.0	147.0±4.0	101.5±1.0	107.5±0.5	104.0±0.8	103.0±0.5
1-135641	40.04	165.0±4.0	168.0±2.0	155.0±3.0	148.0±1.0	164.5±0.5	168.5±0.5	163.5±0.5	166.5±0.5
1-635503	39.05	121.0±1.0	72.0±1.0	82.0±1.0	83.0±1.0	140.0±1.2	145.0±0.5	141.5±0.5	138.5±0.5
1-235398	38.74	154.0±1.0	86.0±2.0	123.0±1.0	120.0±1.0	98.0±0.5	102.0±0.5	99.5±0.5	100.0±0.5
1-259142	40.09	211.0±1.0	272.0±5.0	248.0±4.0	274.0±4.0	102.5±0.5	100.0±0.5	106.5±0.5	101.5±0.5
1-55572	38.93	194.0±2.0	117.0±1.0	208.0±4.0	198.0±5.0	51.0±0.5	52.0±0.5	50.5±0.5	52.0±0.8
1-489649	39.05	170.0±1.0	100.0±2.0	170.0±6.0	155.0±2.0	170.5±1.5	169.0±0.5	1.0±0.5	171.5±0.8
1-109056	40.07	124.0±1.0	104.0±1.0	104.0±1.0	115.0±1.0	157.0±1.5	159.0±0.5	156.0±1.0	154.0±1.0
1-73005	38.81	107.0±1.0	91.0±4.0	91.0±1.0	91.0±1.0	43.5±2.2	59.5±0.5	44.0±1.0	44.0±1.2
1-43009	38.65	94.0±1.0	79.0±2.0	83.0±1.0	85.0±1.0	168.0±1.2	172.5±1.0	171.0±1.0	171.5±1.0
1-24148	40.06	149.0±1.0	126.0±1.0	172.0±1.0	159.0±1.0	155.5±0.8	150.5±0.5	163.5±0.5	134.5±0.5
1-285031	38.95	117.0±1.0	67.0±1.0	83.0±0.0	82.0±0.0	38.0±0.8	38.0±0.5	37.0±0.8	36.5±0.8
1-236099	38.51	85.0±1.0	96.0±3.0	102.0±4.0	83.0±4.0	1.0±1.7	138.0±2.2	37.5±0.5	118.5±0.5
1-166919	39.63	164.0±2.0	158.0±3.0	153.0±4.0	223.0±4.0	105.0±1.0	106.0±0.5	103.0±0.5	102.5±0.8
12-129446	39.24	115.0±1.0	113.0±3.0	84.0±1.0	97.0±2.0	159.0±1.5	161.0±0.5	157.0±1.0	157.5±0.8
1-90849	39.1	115.0±1.0	88.0±2.0	81.0±1.0	95.0±1.0	58.5±1.0	51.5±0.5	55.5±0.5	57.5±0.5
1-248389	39.91	148.0±0.0	144.0±1.0	175.0±1.0	160.0±1.0	177.0±1.5	145.0±0.5	128.5±0.5	145.5±0.5
1-94554	38.98	136.0±1.0	111.0±3.0	135.0±2.0	146.0±5.0	29.5±2.0	37.5±0.5	8.0±0.8	44.0±0.5
1-245774	38.97	130.0±1.0	99.0±2.0	98.0±1.0	107.0±1.0	85.5±1.2	91.5±0.5	85.5±0.8	87.0±0.5
1-321739	39.9	172.0±4.0	145.0±2.0	109.0±1.0	123.0±1.0	172.0±0.5	163.5±0.5	174.0±0.5	179.0±0.5
1-247417	38.77	107.0±1.0	82.0±2.0	85.0±1.0	90.0±1.0	142.0±0.5	141.0±0.5	141.0±0.5	141.5±0.5
1-633994	38.79	238.0±26.0	99.0±2.0	131.0±4.0	201.0±21.0	124.5±0.8	135.5±0.5	123.0±1.0	129.5±0.5
1-234618	39.99	182.0±17.0	167.0±3.0	123.0±9.0	137.0±1.0	23.0±0.5	16.0±1.2	19.0±0.5	23.0±0.8
1-282144	39.16	83.0±1.0	93.0±2.0	70.0±1.0	75.0±1.0	179.0±2.5	163.0±0.5	179.0±1.5	165.5±0.5
1-339125	38.97	181.0±2.0	132.0±3.0	284.0±44.0	653.0±231.0	170.5±1.5	179.5±0.5	141.0±0.5	165.0±0.5
1-229010	39.88	224.0±1.0	237.0±2.0	268.0±4.0	228.0±1.0	177.5±0.5	1.5±0.5	178.0±0.5	0.5±0.5
1-210962	39.01	194.0±1.0	117.0±2.0	147.0±2.0	157.0±2.0	91.5±1.2	96.5±0.5	89.0±0.5	89.5±0.5
1-613211	38.65	242.0±1.0	108.0±3.0	192.0±3.0	188.0±4.0	22.0±0.5	16.5±0.5	18.0±0.5	22.5±0.5
1-211311	39.83	114.0±1.0	173.0±2.0	191.0±2.0	219.0±3.0	160.0±3.0	156.0±0.5	167.5±2.5	166.0±2.0
1-25688	38.35	110.0±1.0	64.0±2.0	110.0±2.0	115.0±1.0	20.5±1.5	13.5±0.5	17.0±0.8	19.5±1.5
1-94422	38.87	129.0±1.0	82.0±1.0	131.0±2.0	123.0±1.0	47.0±1.0	28.0±0.5	49.0±1.0	52.0±0.8
1-373161	39.86	211.0±0.0	139.0±1.0	140.0±1.0	135.0±1.0	124.0±0.5	164.5±0.5	126.0±0.5	33.5±0.5
1-259650	39.47	224.0±1.0	234.0±5.0	161.0±5.0	209.0±50.0	166.5±0.8	170.5±0.5	158.5±0.5	166.0±0.5
1-289865	38.73	271.0±2.0	128.0±10.0	313.0±13.0	213.0±10.0	40.0±1.8	97.5±0.5	58.5±0.5	22.5±0.5
1-210646	39.84	96.0±1.0	108.0±1.0	91.0±1.0	104.0±1.0	106.5±0.8	107.0±1.0	106.5±0.5	106.5±0.8
1-114306	38.65	101.0±1.0	44.0±3.0	95.0±1.0	113.0±3.0	128.5±2.0	135.0±0.8	134.0±0.8	133.5±0.8
1-487130	38.93	75.0±1.0	50.0±2.0	69.0±1.0	84.0±2.0	97.0±1.5	98.0±0.5	90.5±0.5	95.5±0.5

Table A1 – continued

<i>mangaid</i>	$\log_{10} L_{[O\,iii]}$	σ_\star	$\sigma_{[O\,iii]}$	$\sigma_{H\alpha}$	$\sigma_{[N\,ii]}$	$\Psi_0 \star$	Ψ_0 [O III]	Ψ_0 H α	Ψ_0 [N II]
1-351790	39.83	82.0±1.0	88.0±1.0	83.0±1.0	82.0±2.0	135.5±2.2	96.5±1.8	83.5±2.2	91.5±0.8
1-23731	37.83	140.0±1.0	106.0±7.0	264.0±16.0	406.0±54.0	134.0±2.0	145.5±0.8	108.0±0.5	126.5±0.5
1-167334	38.83	111.0±1.0	89.0±1.0	136.0±1.0	138.0±1.0	120.5±2.0	166.5±0.5	11.0±34.5	56.0±4.5
1-163831	39.64	138.0±1.0	173.0±3.0	157.0±4.0	209.0±3.0	95.5±1.2	93.0±0.5	95.5±1.2	97.0±0.5
1-247456	39.3	879.0±34.0	172.0±13.0	1090.0±327.0	749.0±91.0	149.0±1.2	169.0±0.5	167.5±0.8	167.5±0.5
1-210593	39.04	160.0±1.0	128.0±3.0	146.0±4.0	147.0±4.0	101.5±1.0	107.5±0.5	104.0±0.8	103.0±0.5
1-22301	39.84	163.0±2.0	177.0±4.0	137.0±5.0	177.0±5.0	9.5±1.5	8.5±1.8	4.5±0.5	4.0±0.5
1-251871	39.15	160.0±2.0	108.0±5.0	128.0±2.0	127.0±3.0	63.0±0.5	66.0±0.5	63.0±0.5	61.5±1.0
1-72914	39.01	143.0±1.0	101.0±4.0	110.0±2.0	136.0±4.0	72.5±0.8	82.5±0.8	76.0±0.5	74.0±0.5
1-248420	39.71	138.0±1.0	159.0±1.0	152.0±2.0	151.0±2.0	49.5±1.0	49.5±1.0	49.0±1.0	49.0±1.0
1-211063	38.75	136.0±1.0	76.0±2.0	141.0±2.0	111.0±2.0	170.0±1.8	164.0±0.5	166.5±1.8	165.0±1.2
1-211074	38.86	154.0±0.0	126.0±2.0	150.0±2.0	138.0±2.0	142.5±1.0	133.5±0.5	142.5±0.8	143.0±0.8
1-23979	39.72	118.0±1.0	132.0±1.0	115.0±1.0	120.0±1.0	56.5±1.8	67.5±0.5	75.5±0.5	59.0±0.5
1-320681	37.49	189.0±2.0	104.0±22.0	288.0±14.0	306.0±31.0	53.0±0.8	67.0±1.0	53.0±9.8	33.0±0.5
1-519738	38.44	158.0±1.0	101.0±3.0	135.0±7.0	237.0±19.0	56.5±1.0	52.5±0.5	60.0±0.5	52.5±0.5
1-542318	39.88	143.0±1.0	144.0±2.0	172.0±2.0	164.0±2.0	71.0±2.8	119.0±0.5	82.0±0.5	96.0±0.5
1-285052	38.79	143.0±1.0	114.0±4.0	137.0±2.0	110.0±1.0	98.0±2.2	75.0±0.5	93.5±1.2	97.0±1.5
1-377125	38.98	143.0±1.0	99.0±2.0	144.0±4.0	107.0±3.0	136.5±9.0	100.5±0.5	129.0±0.8	129.0±0.5
1-95092	39.75	143.0±1.0	154.0±3.0	130.0±2.0	154.0±2.0	85.5±1.0	80.5±0.5	86.0±0.5	85.5±0.5
1-210962	39.01	194.0±1.0	117.0±2.0	147.0±2.0	157.0±2.0	91.5±1.2	96.5±0.5	89.0±0.5	89.5±0.5
1-251279	39.15	156.0±1.0	120.0±2.0	117.0±2.0	130.0±2.0	150.0±1.0	142.5±0.5	146.0±0.5	146.0±0.5
1-279676	39.54	155.0±1.0	125.0±2.0	120.0±2.0	145.0±2.0	20.0±1.5	27.5±0.5	19.5±0.5	19.5±0.5
1-44789	39.1	154.0±2.0	142.0±3.0	173.0±4.0	148.0±1.0	85.0±0.8	95.0±0.5	88.0±1.5	90.0±0.5
1-378401	39.38	224.0±2.0	223.0±4.0	188.0±7.0	232.0±11.0	162.5±1.0	33.5±0.5	38.0±0.5	26.5±0.5
1-201561	39.59	168.0±2.0	157.0±2.0	168.0±2.0	166.0±1.0	23.5±3.0	22.5±0.5	29.5±0.5	42.5±0.5
1-24246	39.1	110.0±1.0	134.0±4.0	94.0±2.0	105.0±2.0	139.0±1.5	134.0±0.8	134.0±1.0	121.5±0.5
1-285052	38.79	143.0±1.0	114.0±4.0	137.0±2.0	110.0±1.0	98.0±2.2	75.0±0.5	93.5±1.2	97.0±1.5
1-198182	39.68	217.0±1.0	195.0±1.0	219.0±1.0	227.0±2.0	44.5±0.8	35.5±0.8	42.5±0.8	55.0±0.5
1-256185	39.22	214.0±1.0	171.0±10.0	151.0±5.0	202.0±12.0	178.5±0.8	162.5±0.8	167.5±0.8	168.0±1.2
1-48053	–	286.0±1.0	116.0±36.0	184.0±10.0	294.0±13.0	12.0±0.8	161.5±0.5	39.0±0.5	160.0±0.5
1-96075	39.53	122.0±1.0	133.0±2.0	115.0±2.0	137.0±2.0	42.0±0.8	47.5±0.5	43.5±0.5	44.0±0.5
1-166947	38.79	149.0±1.0	83.0±3.0	143.0±3.0	116.0±2.0	36.0±3.2	123.0±0.5	34.0±0.8	35.5±0.8
1-52259	38.98	89.0±1.0	100.0±3.0	63.0±0.0	63.0±0.0	90.5±4.2	103.0±0.5	87.5±12.0	99.5±6.2
1-519742	39.78	96.0±1.0	99.0±0.0	86.0±1.0	80.0±1.0	133.0±4.0	124.5±0.5	129.5±1.8	120.5±1.0
1-37079	37.71	72.0±1.0	39.0±3.0	78.0±1.0	96.0±2.0	157.5±6.0	15.0±0.5	177.5±3.0	25.5±0.5
1-276679	38.42	88.0±1.0	99.0±4.0	61.0±0.0	71.0±0.0	152.0±2.2	137.5±0.5	151.5±0.8	152.5±0.5
1-491229	39.64	189.0±1.0	213.0±5.0	249.0±3.0	226.0±2.0	101.5±1.2	82.5±0.5	99.5±0.5	105.0±0.5
1-94554	38.98	136.0±1.0	111.0±3.0	135.0±2.0	146.0±5.0	29.5±2.0	37.5±0.5	8.0±0.8	44.0±0.5
1-604048	39.14	163.0±1.0	126.0±1.0	124.0±2.0	129.0±3.0	58.5±2.5	71.0±0.5	59.0±1.8	67.0±1.8
1-604761	39.64	193.0±2.0	186.0±3.0	178.0±2.0	189.0±3.0	70.0±0.5	68.0±0.5	66.5±0.5	66.5±0.5
1-210173	39.28	155.0±2.0	137.0±4.0	113.0±2.0	135.0±3.0	122.5±1.0	121.0±0.5	121.0±0.5	124.5±0.5
1-71525	39.0	136.0±1.0	94.0±5.0	242.0±135.0	685.0±263.0	126.5±1.2	138.0±0.5	130.5±0.8	130.5±0.5
1-25725	39.39	190.0±2.0	198.0±3.0	195.0±4.0	225.0±4.0	138.5±2.2	136.5±0.5	133.0±1.2	144.5±0.5
1-211079	38.53	198.0±1.0	228.0±11.0	250.0±18.0	252.0±15.0	178.5±0.8	167.0±0.5	126.5±0.5	125.5±0.5
1-322074	38.12	120.0±0.0	93.0±3.0	227.0±13.0	234.0±49.0	35.5±2.5	68.5±0.5	120.0±0.5	160.5±0.5
1-94604	39.5	110.0±1.0	109.0±1.0	136.0±4.0	343.0±54.0	153.0±2.0	166.0±0.5	157.5±0.5	144.0±0.5
1-295095	38.76	101.0±1.0	112.0±3.0	80.0±1.0	88.0±2.0	1.0±2.2	3.0±0.8	178.0±1.5	1.0±1.2
1-134239	39.17	138.0±1.0	136.0±3.0	119.0±3.0	140.0±3.0	32.5±1.5	31.5±0.5	34.0±1.5	35.5±1.5

Table A1 – continued

mangaid	$\log_{10} L_{[O\,iii]}$	σ_\star	$\sigma_{[O\,iii]}$	$\sigma_{H\alpha}$	$\sigma_{[N\,ii]}$	$\Psi_0 \star$	Ψ_0 [O III]	Ψ_0 H α	Ψ_0 [N II]
1-37036	39.42	220.0 ± 1.0	173.0 ± 2.0	206.0 ± 2.0	197.0 ± 3.0	98.0 ± 0.8	86.0 ± 0.5	84.0 ± 0.5	99.0 ± 0.5
1-210785	37.08	165.0 ± 1.0	102.0 ± 12.0	569.0 ± 171.0	2128.0 ± 444.0	125.5 ± 0.8	130.0 ± 0.5	113.5 ± 0.5	107.0 ± 0.5
1-25680	39.08	230.0 ± 1.0	140.0 ± 3.0	176.0 ± 3.0	189.0 ± 4.0	55.5 ± 2.0	168.0 ± 0.5	1.0 ± 0.5	174.5 ± 0.5
1-167688	39.56	96.0 ± 1.0	81.0 ± 0.0	95.0 ± 0.0	89.0 ± 1.0	35.5 ± 9.2	18.0 ± 1.0	40.0 ± 0.8	70.5 ± 1.5
1-235587	38.59	125.0 ± 0.0	84.0 ± 1.0	105.0 ± 2.0	106.0 ± 2.0	85.5 ± 2.2	92.0 ± 0.5	99.0 ± 1.8	100.0 ± 1.0
1-37062	39.02	79.0 ± 1.0	83.0 ± 1.0	91.0 ± 1.0	96.0 ± 1.0	21.5 ± 3.5	173.0 ± 0.5	19.0 ± 12.0	31.0 ± 0.5
1-279666	39.45	115.0 ± 1.0	103.0 ± 1.0	104.0 ± 1.0	121.0 ± 1.0	57.5 ± 2.2	52.0 ± 0.5	60.0 ± 1.8	46.5 ± 1.5
1-392976	38.57	108.0 ± 1.0	94.0 ± 3.0	133.0 ± 5.0	123.0 ± 4.0	16.0 ± 0.5	56.0 ± 0.5	80.5 ± 0.5	166.0 ± 0.5
1-47499	38.86	110.0 ± 0.0	102.0 ± 3.0	128.0 ± 4.0	121.0 ± 4.0	108.0 ± 2.2	82.5 ± 1.8	108.0 ± 0.5	126.0 ± 0.5
1-339163	39.35	159.0 ± 1.0	323.0 ± 6.0	245.0 ± 4.0	353.0 ± 8.0	38.5 ± 0.5	42.0 ± 0.5	39.0 ± 0.5	39.0 ± 0.5
1-136125	38.56	109.0 ± 1.0	61.0 ± 2.0	118.0 ± 2.0	112.0 ± 2.0	68.0 ± 0.5	69.0 ± 0.5	67.5 ± 0.5	67.5 ± 0.5
1-626830	38.62	137.0 ± 1.0	107.0 ± 3.0	115.0 ± 2.0	136.0 ± 2.0	22.5 ± 0.5	29.5 ± 0.5	22.5 ± 0.5	19.5 ± 0.5
1-258774	39.4	143.0 ± 0.0	114.0 ± 2.0	110.0 ± 1.0	135.0 ± 0.0	154.0 ± 4.2	152.0 ± 1.2	155.0 ± 3.2	172.5 ± 3.8
1-379660	39.12	139.0 ± 1.0	132.0 ± 3.0	118.0 ± 4.0	127.0 ± 4.0	115.5 ± 1.2	106.0 ± 0.5	111.5 ± 0.8	113.5 ± 0.5
1-48208	38.7	162.0 ± 1.0	94.0 ± 2.0	140.0 ± 4.0	91.0 ± 5.0	71.5 ± 2.2	75.0 ± 0.5	76.0 ± 0.5	66.5 ± 0.5
1-198153	39.29	176.0 ± 1.0	145.0 ± 2.0	177.0 ± 1.0	178.0 ± 1.0	93.5 ± 0.5	96.0 ± 0.5	94.5 ± 0.5	94.5 ± 0.5
1-211063	38.75	136.0 ± 1.0	76.0 ± 2.0	141.0 ± 2.0	111.0 ± 2.0	170.0 ± 1.8	164.0 ± 0.5	166.5 ± 1.8	165.0 ± 1.2
1-135810	38.45	112.0 ± 1.0	80.0 ± 2.0	95.0 ± 2.0	101.0 ± 2.0	52.0 ± 0.8	54.5 ± 0.5	50.5 ± 0.8	50.5 ± 0.5
1-91016	39.49	103.0 ± 1.0	125.0 ± 2.0	138.0 ± 3.0	173.0 ± 4.0	50.5 ± 4.0	44.5 ± 1.2	51.5 ± 1.2	57.0 ± 2.0
1-338828	39.3	94.0 ± 1.0	90.0 ± 1.0	80.0 ± 1.0	80.0 ± 1.0	103.0 ± 0.5	101.5 ± 0.5	96.0 ± 0.5	86.0 ± 1.2
1-386695	39.68	105.0 ± 2.0	119.0 ± 1.0	105.0 ± 1.0	107.0 ± 1.0	129.0 ± 1.2	88.0 ± 0.5	141.5 ± 0.5	89.5 ± 0.5
1-279073	39.34	231.0 ± 1.0	161.0 ± 4.0	186.0 ± 2.0	181.0 ± 3.0	15.0 ± 1.5	169.5 ± 0.8	155.5 ± 0.5	164.0 ± 0.5
1-211100	38.09	198.0 ± 1.0	116.0 ± 7.0	275.0 ± 44.0	346.0 ± 14.0	152.0 ± 4.8	127.0 ± 0.5	103.0 ± 0.5	165.0 ± 0.5
1-210784	38.3	171.0 ± 0.0	97.0 ± 4.0	159.0 ± 2.0	218.0 ± 3.0	90.0 ± 2.2	101.0 ± 0.5	59.0 ± 1.2	62.5 ± 0.5
1-135044	39.44	115.0 ± 1.0	116.0 ± 2.0	156.0 ± 2.0	167.0 ± 3.0	95.5 ± 1.2	96.5 ± 0.5	96.5 ± 1.2	98.5 ± 0.5
1-218280	38.7	148.0 ± 0.0	104.0 ± 1.0	121.0 ± 1.0	114.0 ± 3.0	99.0 ± 1.0	96.0 ± 0.5	98.0 ± 0.5	98.0 ± 0.5
1-211063	38.75	136.0 ± 1.0	76.0 ± 2.0	141.0 ± 2.0	111.0 ± 2.0	170.0 ± 1.8	164.0 ± 0.5	166.5 ± 1.8	165.0 ± 1.2
1-148068	39.21	156.0 ± 1.0	121.0 ± 4.0	169.0 ± 2.0	156.0 ± 1.0	63.5 ± 0.8	59.0 ± 0.5	65.0 ± 0.8	66.5 ± 0.5
1-166947	38.79	149.0 ± 1.0	83.0 ± 3.0	143.0 ± 3.0	116.0 ± 2.0	36.0 ± 3.2	123.0 ± 0.5	34.0 ± 0.8	35.5 ± 0.8
1-55572	38.93	194.0 ± 2.0	117.0 ± 1.0	208.0 ± 4.0	198.0 ± 5.0	51.0 ± 0.5	52.0 ± 0.5	50.5 ± 0.5	52.0 ± 0.8
1-277552	39.27	118.0 ± 1.0	119.0 ± 1.0	99.0 ± 1.0	112.0 ± 1.0	3.5 ± 0.5	4.0 ± 0.5	2.5 ± 0.5	2.5 ± 0.8
1-264513	39.28	99.0 ± 1.0	106.0 ± 1.0	77.0 ± 0.0	85.0 ± 1.0	0.5 ± 0.5	177.0 ± 3.8	175.5 ± 1.5	175.5 ± 2.0
1-136125	38.56	109.0 ± 1.0	61.0 ± 2.0	118.0 ± 2.0	112.0 ± 2.0	68.0 ± 0.5	69.0 ± 0.5	67.5 ± 0.5	67.5 ± 0.5
1-217050	39.05	203.0 ± 1.0	154.0 ± 2.0	200.0 ± 2.0	208.0 ± 3.0	60.5 ± 0.5	83.0 ± 0.5	82.0 ± 0.5	78.0 ± 0.5
1-135372	38.66	212.0 ± 1.0	183.0 ± 6.0	1011.0 ± 363.0	280.0 ± 13.0	20.0 ± 0.8	23.0 ± 0.5	22.5 ± 0.5	29.5 ± 0.5
1-274663	38.87	216.0 ± 1.0	125.0 ± 3.0	188.0 ± 3.0	188.0 ± 5.0	153.5 ± 1.8	163.5 ± 0.5	111.5 ± 0.5	155.5 ± 0.5
1-25554	38.96	114.0 ± 0.0	111.0 ± 1.0	117.0 ± 1.0	112.0 ± 2.0	74.5 ± 1.2	67.5 ± 0.5	76.5 ± 0.5	82.0 ± 0.5
1-135625	39.33	98.0 ± 1.0	111.0 ± 2.0	98.0 ± 1.0	98.0 ± 1.0	17.5 ± 1.2	16.0 ± 1.5	15.0 ± 0.5	12.5 ± 1.0
1-216958	38.9	99.0 ± 0.0	78.0 ± 0.0	67.0 ± 0.0	72.0 ± 0.0	58.0 ± 5.8	41.0 ± 0.5	60.0 ± 4.5	81.5 ± 0.5
1-135285	38.93	133.0 ± 1.0	155.0 ± 2.0	166.0 ± 2.0	162.0 ± 1.0	116.5 ± 0.5	112.0 ± 0.5	114.0 ± 0.5	113.0 ± 0.5
1-633990	38.77	97.0 ± 0.0	93.0 ± 1.0	99.0 ± 0.0	103.0 ± 1.0	33.5 ± 1.2	30.0 ± 0.5	31.5 ± 0.5	37.5 ± 0.5
1-25688	38.35	110.0 ± 1.0	64.0 ± 2.0	110.0 ± 2.0	115.0 ± 1.0	20.5 ± 1.5	13.5 ± 0.5	17.0 ± 0.8	19.5 ± 1.5

This paper has been typeset from a TeX/LaTeX file prepared by the author.

Table A2. Parameters of AGN in MaNGA-MPL5. (1) galaxy identification in the MaNGA survey; (2)-(3): RA/DEC (2000) in degrees; (4) spectroscopic redshift from SDSS-III; (5): integrated absolute r -band magnitude from SDSS-III; (6): stellar mass in units of M_{\odot} ; errors associated to the stellar masses of galaxies in our sample are typically under 0.03 dex (Conroy, Gunn & White, 2009); (7) elliptical/spiral/merging classification from Galaxy Zoo I; (8)-(9): r -band concentration and asymmetry; (10) [OIII] luminosity in units of 10^{40} erg s $^{-1}$. Table extracted of Rembold et al. (2017).

mangalID (1)	RA (2)	DEC (3)	z (4)	M_r (5)	$\log M^*/M_{\odot}$ (6)	GZ1 _c (7)	C (8)	A (9)	$L(\text{[OIII]})$ (10)
1-558912	166.129410	42.624554	0.1261	-20.46	11.25	—	0.37	0.12	56.82±1.25
1-269632	247.560974	26.206474	0.1315	-21.78	11.62	S	0.47	0.05	30.08±1.69
1-258599	186.181000	44.410770	0.1256	-21.24	11.68	E	0.50	0.11	20.95±0.67
1-72322	121.014198	40.802612	0.1262	-21.81	12.05	S	0.34	0.08	20.66±0.43
1-121532	118.091110	34.326569	0.1400	-20.51	11.34	E	0.33	0.05	11.68±0.96
1-209980	240.470871	45.351940	0.0420	-19.70	10.79	S	0.57	0.04	11.01±0.17
1-44379	120.700706	45.034554	0.0389	-19.89	10.97	S	0.24	0.06	8.94±0.14
1-149211	168.947800	50.401634	0.0473	-18.27	10.16	S	0.29	0.03	7.88±0.14
1-173958	167.306015	49.519432	0.0724	-20.53	11.31	S	0.33	0.06	6.79±0.30
1-338922	114.775749	44.402767	0.1345	-20.27	11.13	M	0.44	0.03	6.77±0.90
1-279147	168.957733	46.319565	0.0533	-19.51	10.66	S	0.45	0.03	6.77±0.20
1-460812	127.170799	17.581400	0.0665	-19.81	11.44	—	0.38	0.05	6.46±0.31
1-92866	243.581818	50.465611	0.0603	-20.56	11.69	E	0.49	0.05	6.12±0.30
1-94784	249.318420	44.418228	0.0314	-20.06	10.85	S	0.42	0.03	5.96±0.12
1-44303	119.182152	44.856709	0.0499	-19.72	10.62	S	0.29	0.10	5.56±0.12
1-339094	117.472420	45.248482	0.0313	-19.02	10.52	E	0.36	0.03	5.29±0.09
1-137883	137.874756	45.468319	0.0268	-18.06	10.77	E/S	0.41	0.01	3.87±0.12
1-48116	132.653992	57.359669	0.0261	-19.18	10.60	S	0.31	0.06	3.79±0.08
1-256446	166.509872	43.173473	0.0584	-19.40	11.14	E	0.49	0.05	3.74±0.15
1-95585	255.029877	37.839500	0.0633	-20.88	11.24	S	0.27	0.08	3.58±0.16
1-135641	249.557312	40.146820	0.0304	-19.03	11.19	S	0.28	0.08	3.52±0.09
1-259142	193.703995	44.155567	0.0543	-20.75	11.29	S	0.39	0.06	3.47±0.20
1-109056	39.446587	0.405085	0.0473	-19.27	10.57	—	0.32	0.05	3.24±0.08
1-24148	258.827423	57.658772	0.0282	-18.51	10.56	S	0.31	0.04	3.17±0.05
1-166919	146.709106	43.423843	0.0722	-20.85	11.28	S	0.37	0.06	2.64±0.25
1-248389	240.658051	41.293427	0.0348	-19.36	10.57	S	0.49	0.12	2.55±0.09
1-321739	226.431656	44.404903	0.0283	-18.91	11.12	S	0.40	0.14	2.24±0.10
1-234618	202.128433	47.714039	0.0608	-19.64	11.37	S	0.31	0.09	2.23±0.23
1-229010	57.243038	-1.144831	0.0407	-20.51	11.46	—	0.41	0.03	2.11±0.09
1-211311	248.426392	39.185120	0.0298	-19.04	10.44	E/S	0.43	0.02	1.99±0.06
1-373161	222.810074	30.692245	0.0547	-21.30	11.60	E	0.43	0.00	1.87±0.11
1-210646	245.157181	41.466873	0.0606	-20.38	10.98	S	0.18	0.05	1.80±0.10
1-351790	121.147926	50.708557	0.0227	-18.09	9.92	E	0.39	0.02	1.72±0.03
1-163831	118.627846	25.815987	0.0631	-20.84	11.26	S	0.27	0.05	1.67±0.13
1-22301	253.405563	63.031269	0.1052	-21.19	11.18	S	0.29	0.08	1.67±0.23
1-248420	241.823395	41.403603	0.0346	-19.71	10.90	S	0.21	0.07	1.66±0.06
1-23979	258.158752	57.322422	0.0266	-18.27	10.42	E	0.44	0.06	1.60±0.05
1-542318	245.248306	49.001778	0.0582	-19.75	10.91	E	0.34	0.01	1.58±0.07
1-95092	250.846420	39.806461	0.0302	-19.95	11.20	E	0.47	0.04	1.54±0.07
1-279676	173.981888	48.021458	0.0587	-19.40	10.81	—	0.32	0.02	1.52±0.14
1-201561	118.053215	28.772579	0.0637	-19.73	10.88	S	0.30	0.07	1.37±0.15
1-198182	224.749649	48.409855	0.0359	-20.22	11.09	E	0.49	0.01	1.34±0.11
1-96075	253.946381	39.310535	0.0631	-21.12	11.35	S	0.29	0.07	1.26±0.13
1-519742	206.612457	22.076742	0.0276	-17.62	9.64	S	0.23	0.04	1.19±0.03
1-491229	172.607544	22.216530	0.0393	-20.25	11.12	E	0.51	0.02	1.14±0.11
1-604761	113.472275	37.025906	0.0618	-20.92	11.34	S	0.26	0.12	1.00±0.13
1-25725	262.996735	59.971638	0.0291	-18.30	10.55	E	0.44	0.04	0.92±0.05
1-94604	251.335938	42.757790	0.0493	-19.44	10.52	S	0.37	0.01	0.86±0.07
1-37036	41.699909	0.421577	0.0283	-19.02	10.66	E	0.40	0.09	0.84±0.06
1-167688	155.885559	46.057755	0.0258	-17.86	9.75	E	0.52	0.04	0.84±0.02
1-279666	173.911240	47.515518	0.0455	-18.83	10.42	E	0.31	0.02	0.84±0.07
1-339163	116.280205	46.072422	0.0312	-20.02	10.97	S	0.30	0.10	0.82±0.07
1-258774	186.400864	45.083858	0.0384	-19.60	10.77	—	0.55	0.03	0.77±0.10
1-198153	224.289078	48.633968	0.0354	-19.83	11.00	S	0.27	0.07	0.76±0.08
1-91016	234.810974	56.670856	0.0463	-18.60	10.56	S	0.27	0.06	0.76±0.09
1-279073	170.588150	46.430504	0.0323	-19.53	10.79	E	0.51	0.01	0.63±0.06
1-135044	247.907990	41.493645	0.0303	-19.76	10.65	S	0.31	0.05	0.61±0.04

Table A2 – continued

mangaID (1)	RA (2)	DEC (3)	z (4)	M_r (5)	$\log M^{\star}/M_{\odot}$ (6)	GZ1 _c (7)	C (8)	A (9)	$L(\text{[OIII]})$ (10)
1-148068	156.805679	48.244793	0.0610	-20.72	11.41	S	0.22	0.04	0.45±0.15
1-277552	167.034561	45.984623	0.0362	-19.72	10.83	S	0.21	0.15	0.44±0.05
1-217050	136.719986	41.408253	0.0274	-19.66	10.93	E	0.47	0.02	0.43±0.03
1-25554	262.486053	58.397408	0.0268	-19.27	10.52	S	0.36	0.04	0.24±0.03
1-135285	247.216949	42.812012	0.0316	-19.66	10.78	–	0.32	0.05	0.20±0.04

Table A3. Control sample parameters. (1) identification of the AGN host associated to the control galaxy; (2)-(11) same as (1)-(10) of Table A2. Twelve control sample objects have been paired to two different AGN hosts and appear more than once in the table. Table extracted of Rembold et al. (2017).

AGN mangaID (1)	mangaID (2)	RA (3)	DEC (4)	z (5)	M_r (6)	$\log M^*/M_\odot$ (7)	GZ1 _c (8)	C (9)	A (10)	$L(\text{[OIII]})$ (11)
1-558912	1-71481	117.456001	34.883911	0.1312	-20.95	11.70	E	0.47	0.02	0.10±0.20
	1-72928	127.256485	45.016773	0.1270	-20.62	11.52	E	0.40	0.21	0.09±0.23
1-269632	1-210700	248.140564	39.131020	0.1303	-20.96	11.67	S	0.36	0.03	1.55±0.44
	1-378795	118.925613	50.172771	0.0967	-20.77	11.35	S	0.32	0.03	0.72±0.31
1-258599	1-93876	246.942947	44.177521	0.1394	-20.75	11.50	E	0.44	0.01	0.46±0.36
	1-166691	146.047348	42.900040	0.1052	-20.50	11.36	E	0.51	0.04	0.09±0.49
1-72322	1-121717	118.803429	35.596798	0.1098	-21.11	11.61	S	0.39	0.12	1.40±0.57
	1-43721	116.967567	43.383499	0.1114	-21.41	11.86	S	0.32	0.01	1.91±0.52
1-121532	1-218427	124.342316	27.796206	0.1496	-21.30	11.47	E	0.47	0.04	0.72±0.62
	1-177493	257.085754	31.746916	0.1081	-20.90	11.30	E	0.38	0.06	2.29±0.28
1-209980	1-295095	248.348663	24.776577	0.0410	-18.40	10.14	E	0.35	0.05	0.15±0.03
	1-92626	241.799545	48.572563	0.0434	-20.04	11.04	S	0.36	0.03	0.76±0.07
1-44379	1-211082	247.620041	39.626045	0.0304	-19.72	11.07	E	0.31	0.06	0.19±0.04
	1-135371	250.156235	39.221634	0.0352	-19.20	10.76	S	0.28	0.11	0.25±0.07
1-149211	1-377321	110.556152	42.183643	0.0444	-19.02	9.89	S	0.31	0.03	4.53±0.13
	1-491233	172.563995	22.992010	0.0332	-18.39	10.59	S	0.29	0.06	0.25±0.03
1-173958	1-247456	232.823196	45.416538	0.0705	-20.05	10.83	–	0.40	0.02	0.57±0.16
	1-24246	264.840790	56.567070	0.0818	-19.91	10.57	S	0.75	0.36	0.11±0.06
1-338922	1-286804	211.904861	44.482269	0.1429	-20.03	10.50	M	0.44	0.32	2.23±0.43
	1-109493	56.425140	-0.378460	0.1093	-20.46	11.26	–	0.49	-0.01	0.15±0.18
1-279147	1-283246	191.078873	46.407131	0.0496	-19.17	10.55	S	0.47	0.04	0.23±0.06
	1-351538	119.145126	47.563850	0.0692	-19.67	11.00	S	0.35	0.08	0.46±0.13
1-460812	1-270160	248.274612	26.211815	0.0660	-20.37	11.46	S	0.50	0.02	0.70±0.39
	1-258455	183.612198	45.195454	0.0653	-20.02	11.03	E	0.40	0.03	0.49±0.14
1-92866	1-94514	248.241180	42.524670	0.0614	-20.60	11.17	E	0.51	0.00	–
	1-210614	244.501755	41.392189	0.0612	-20.64	11.48	E	0.49	0.01	0.40±0.14
1-94784	1-211063	247.058411	40.313835	0.0331	-19.87	10.79	S	0.33	0.09	0.20±0.04
	1-135502	247.764175	39.838505	0.0305	-19.51	11.13	S	0.40	0.09	0.50±0.05
1-44303	1-339028	116.097923	44.527740	0.0497	-20.01	11.24	S	0.36	0.06	0.44±0.08
	1-379087	119.910118	51.792362	0.0534	-19.60	11.02	S	0.38	0.10	0.72±0.13
1-339094	1-274646	158.017029	43.859268	0.0284	-18.70	10.36	E	0.53	0.02	0.35±0.04
	1-24099	258.027618	57.504009	0.0282	-18.67	10.34	E	0.44	0.01	0.06±0.03
1-137883	1-178838	312.023621	0.068841	0.0247	-17.54	10.46	–	0.51	0.19	0.10±0.02
	1-36878	42.542126	-0.867116	0.0232	-18.88	10.77	E	0.45	0.07	0.28±0.04
1-48116	1-386452	136.228333	28.384314	0.0269	-19.54	10.57	S	0.49	0.09	0.32±0.04
	1-24416	263.033173	56.878746	0.0281	-19.16	10.66	S	0.37	0.03	0.22±0.03
1-256446	1-322671	235.797028	39.238773	0.0637	-19.77	10.82	E	0.49	0.04	–
	1-256465	166.752243	43.089901	0.0575	-19.70	10.79	E	0.50	0.01	0.59±0.11
1-95585	1-166947	147.335007	43.442989	0.0720	-20.79	10.81	S	0.29	0.02	0.13±0.08
	1-210593	244.419754	41.899155	0.0605	-19.76	10.90	S	0.36	0.06	0.43±0.14
1-135641	1-635503	318.990448	9.543076	0.0293	-19.37	10.91	S	0.22	0.10	0.15±0.06
	1-235398	213.149185	47.253059	0.0281	-18.91	10.99	S	0.28	0.10	0.16±0.05
1-259142	1-55572	133.121307	56.112690	0.0454	-20.11	11.03	S	0.40	0.06	0.12±0.04
	1-489649	171.954834	21.386103	0.0406	-19.94	10.95	S	0.40	0.03	0.30±0.08
1-109056	1-73005	125.402306	45.585476	0.0514	-19.47	10.65	S	0.31	0.05	0.20±0.06
	1-43009	113.553879	39.076836	0.0510	-19.41	10.43	S	0.26	0.03	0.12±0.04
1-24148	1-285031	198.701370	47.351547	0.0303	-18.47	10.72	S	0.34	0.05	0.26±0.04
	1-236099	225.236221	41.566265	0.0205	-17.36	9.91	S	0.33	0.04	0.07±0.01
1-166919	12-129446	203.943542	26.101791	0.0670	-20.57	11.32	S	0.34	0.03	0.28±0.09
	1-90849	237.582748	56.131981	0.0661	-20.39	11.16	E	0.30	0.04	0.28±0.05
1-248389	1-94554	248.914688	42.461296	0.0318	-18.96	10.57	S	0.55	0.07	0.22±0.04
	1-245774	214.863297	54.100300	0.0426	-20.22	10.83	S	0.40	0.08	0.29±0.07
1-321739	1-247417	233.319382	45.698528	0.0294	-19.25	10.76	S	0.28	0.09	0.16±0.04
	1-633994	247.419952	40.686954	0.0305	-18.27	11.04	S	0.39	0.11	0.36±0.09
1-234618	1-282144	184.592514	46.155350	0.0492	-18.92	10.31	S	0.21	0.08	0.10±0.02
	1-339125	117.739944	45.989529	0.0534	-18.97	11.17	S	0.35	0.05	0.45±0.23
1-229010	1-210962	246.358719	39.870697	0.0290	-20.49	11.09	S	0.47	0.07	0.35±0.06
	1-613211	167.861847	22.970764	0.0323	-19.87	11.32	E	0.48	0.04	0.16±0.06

Table A3 – continued

AGN mangaID (1)	mangaID (2)	RA (3)	DEC (4)	z (5)	M_r (6)	$\log M^*/M_\odot$ (7)	GZ1 _c (8)	C (9)	A (10)	$L([\text{OIII}])$ (11)
1-211311	1-25688	261.284851	58.764687	0.0292	-18.79	10.32	S	0.29	0.06	0.10±0.02
	1-94422	250.453201	41.818737	0.0316	-19.15	10.55	S	0.37	0.05	0.24±0.03
1-373161	1-259650	196.611053	45.289001	0.0509	-21.07	11.68	E	0.44	0.06	0.67±0.20
	1-289865	322.048584	0.299885	0.0525	-20.90	11.35	–	0.49	0.02	0.11±0.09
1-210646	1-114306	323.742737	11.296529	0.0637	-20.58	10.83	S	0.26	0.05	0.33±0.16
	1-487130	164.447296	21.233431	0.0587	-20.47	10.86	S	0.26	0.11	0.27±0.10
1-351790	1-23731	260.746704	60.559292	0.0205	-18.20	10.19	E	0.40	0.02	0.02±0.01
	1-167334	151.894836	46.093983	0.0243	-18.89	10.60	E	0.43	0.04	0.47±0.05
1-163831	1-247456	232.823196	45.416538	0.0705	-20.05	10.83	–	0.40	0.02	0.57±0.16
	1-210593	244.419754	41.899155	0.0605	-19.76	10.90	S	0.36	0.06	0.43±0.14
1-22301	1-251871	214.506760	41.827644	0.1027	-21.17	11.68	S	0.26	0.05	0.24±0.18
	1-72914	127.580818	45.075867	0.0970	-20.88	11.31	S	0.23	0.08	0.13±0.07
1-248420	1-211063	247.058411	40.313835	0.0331	-19.87	10.79	S	0.33	0.09	0.20±0.04
	1-211074	247.462692	39.766510	0.0318	-19.71	10.79	S	0.30	0.18	0.20±0.04
1-23979	1-320681	213.813095	47.873344	0.0279	-18.76	10.77	E	0.48	0.01	0.09±0.07
	1-519738	206.514709	22.118843	0.0277	-19.49	10.73	E	0.45	0.03	0.11±0.04
1-542318	1-285052	199.061493	47.599365	0.0573	-19.77	10.85	S	0.32	0.04	0.11±0.03
	1-377125	112.221359	41.307812	0.0585	-19.67	10.84	S	0.41	0.02	0.57±0.14
1-95092	1-210962	246.358719	39.870697	0.0290	-20.49	11.09	S	0.47	0.07	0.35±0.06
	1-251279	209.251984	43.362034	0.0329	-20.11	10.97	E	0.47	0.04	0.37±0.06
1-279676	1-44789	120.890366	47.892406	0.0586	-19.33	10.92	–	0.31	0.13	0.32±0.09
	1-378401	117.904335	48.000526	0.0612	-19.65	11.02	E	0.41	0.02	0.57±0.14
1-201561	1-24246	264.840790	56.567070	0.0818	-19.91	10.57	S	0.75	0.36	0.11±0.06
	1-285052	199.061493	47.599365	0.0573	-19.77	10.85	S	0.32	0.04	0.11±0.03
1-198182	1-256185	165.568695	44.271709	0.0370	-20.00	11.03	E	0.50	0.06	0.25±0.04
	1-48053	132.595016	55.378742	0.0308	-20.24	11.49	E	0.50	0.01	–
1-96075	1-166947	147.335007	43.442989	0.0720	-20.79	10.81	S	0.29	0.02	0.13±0.08
	1-52259	59.411037	-6.274680	0.0678	-20.69	11.12	S	0.23	0.07	0.30±0.09
1-519742	1-37079	42.092335	0.986465	0.0274	-17.25	9.55	E	0.27	0.02	0.02±0.01
	1-276679	161.272629	44.054291	0.0253	-18.27	10.10	S	0.24	0.03	0.05±0.01
1-491229	1-94554	248.914688	42.461296	0.0318	-18.96	10.57	S	0.55	0.07	0.22±0.04
	1-604048	50.536137	-0.836265	0.0365	-20.37	10.91	S	0.42	0.09	0.39±0.08
1-604761	1-210173	241.341766	42.488312	0.0778	-20.71	11.10	S	0.33	0.07	0.52±0.13
	1-71525	118.344856	36.274380	0.0457	-20.17	10.97	S	0.27	0.10	0.19±0.06
1-25725	1-211079	247.438034	39.810539	0.0304	-18.97	10.54	E	0.54	0.01	0.03±0.04
	1-322074	228.700729	43.665970	0.0274	-18.15	10.10	E	0.45	0.02	–
1-94604	1-295095	248.348663	24.776577	0.0410	-18.40	10.14	E	0.35	0.05	0.15±0.03
	1-134239	241.416443	46.846561	0.0571	-19.83	10.70	S	0.36	0.04	0.23±0.06
1-37036	1-210785	246.765076	39.527386	0.0338	-20.22	10.97	E	0.47	0.01	–
	1-25680	261.968872	60.097275	0.0278	-19.41	10.84	E	0.52	0.02	0.34±0.04
1-167688	1-235587	214.854660	45.864250	0.0267	-18.88	10.48	E	0.44	0.01	0.08±0.02
	1-37062	41.846367	0.058757	0.0248	-18.30	10.40	E	0.49	0.03	0.27±0.03
1-279666	1-392976	156.428894	37.497524	0.0432	-17.91	10.09	E	0.37	0.02	0.10±0.03
	1-47499	132.037582	54.309921	0.0461	-18.53	10.51	E	0.27	0.04	0.15±0.06
1-339163	1-136125	254.044144	34.836521	0.0316	-19.33	10.50	S	0.25	0.09	0.08±0.02
	1-626830	204.683838	26.328539	0.0282	-19.23	10.67	S	0.28	0.07	0.15±0.04
1-258774	1-379660	119.973717	55.374817	0.0357	-19.44	10.74	E	0.47	0.03	0.37±0.07
	1-48208	134.008118	57.390965	0.0406	-19.57	10.85	S	0.50	0.01	0.12±0.04
1-198153	1-211063	247.058411	40.313835	0.0331	-19.87	10.79	S	0.33	0.09	0.20±0.04
	1-135810	250.123138	39.235115	0.0297	-19.38	10.59	S	0.24	0.09	0.08±0.02
1-91016	1-338828	115.641609	44.215858	0.0418	-18.10	10.42	S	0.28	0.03	0.43±0.05
	1-386695	137.983505	27.899269	0.0474	-19.33	10.48	S	0.27	0.09	0.81±0.09
1-279073	1-211100	247.830322	39.744129	0.0309	-19.15	10.62	E	0.56	0.02	–
	1-210784	247.097122	39.570305	0.0292	-19.61	10.86	E	0.48	0.00	0.15±0.05
1-135044	1-218280	124.003311	27.075895	0.0255	-19.57	10.81	S	0.27	0.08	0.12±0.03
	1-211063	247.058411	40.313835	0.0331	-19.87	10.79	S	0.33	0.09	0.20±0.04
1-148068	1-166947	147.335007	43.442989	0.0720	-20.79	10.81	S	0.29	0.02	0.13±0.08
	1-55572	133.121307	56.112690	0.0454	-20.11	11.03	S	0.40	0.06	0.12±0.04

Table A3 – *continued*

AGN mangaID (1)	mangaID (2)	RA (3)	DEC (4)	z (5)	M_r (6)	$\log M^\star/M_\odot$ (7)	GZ1 _c (8)	C (9)	A (10)	$L([\text{OIII}])$ (11)
1-277552	1-264513	236.941513	28.641697	0.0333	-20.92	11.28	S	0.25	0.18	0.33 ± 0.05
	1-136125	254.044144	34.836521	0.0316	-19.33	10.50	S	0.25	0.09	0.08 ± 0.02
1-217050	1-135372	250.116714	39.320118	0.0301	-20.29	11.08	E	0.49	0.02	0.01 ± 0.23
	1-274663	157.660522	44.012722	0.0280	-19.88	11.00	E	0.50	0.01	0.08 ± 0.02
1-25554	1-135625	248.507462	41.347946	0.0284	-19.06	10.56	S	0.43	0.05	0.56 ± 0.04
	1-216958	136.200287	40.591721	0.0270	-18.95	10.41	S	0.51	0.03	0.23 ± 0.02
1-135285	1-633990	247.304123	41.150871	0.0296	-19.06	10.46	S	0.34	0.03	0.25 ± 0.03
	1-25688	261.284851	58.764687	0.0292	-18.79	10.32	S	0.29	0.06	0.10 ± 0.02